

Reciprocity and Normality in the Scattering Matrix of Disordered Media

by

Shreyas K. Bharadwaj

B.S., University of California, Los Angeles, 2023

Submitted to the Department of Electrical Engineering and Computer Science
in partial fulfillment of the requirements for the degree of

MASTER OF SCIENCE

at the

MASSACHUSETTS INSTITUTE OF TECHNOLOGY

September 2025

© 2025 Shreyas K. Bharadwaj. All rights reserved.

The author hereby grants to MIT a nonexclusive, worldwide, irrevocable, royalty-free license to exercise any and all rights under copyright, including to reproduce, preserve, distribute and publicly display copies of the thesis, or release the thesis under an open-access license.

Authored by: Shreyas K. Bharadwaj
Department of Electrical Engineering and Computer Science
August 15, 2025

Certified by: Martin Villiger
Assistant Professor of Dermatology, Thesis Supervisor

Accepted by: Leslie Kolodziejcki
Professor of Electrical Engineering
Chair, Department Committee on Graduate Students

Reciprocity and Normality in the Scattering Matrix of Disordered Media

by

Shreyas K. Bharadwaj

Submitted to the Department of Electrical Engineering and Computer Science
on August 15, 2025 in partial fulfillment of the requirements for the degree of

MASTER OF SCIENCE

ABSTRACT

The scattering matrix formalism provides a practical characterization of wave transport in linear, source-free systems by relating a set of operationally defined input and output spatial channels. The matrix is structured as a block operator, with diagonal blocks encoding same-side reflection matrices (RMs) and off-diagonal blocks encoding transmission matrices (TMs) in opposing propagation directions. Under Helmholtz reciprocity, symmetry relations are imposed: RMs are symmetric, and forward and reverse TMs are mathematical transposes of each other. These relations were employed as constraints to correct system-induced aberrations in measured scattering matrices of complex optical media via a matrix-based gradient descent procedure. Resulting phase corrections corresponded closely with classical aberration modes without heuristic parameterizations, suggesting that these modes naturally arise to restore reciprocity-induced symmetry. Vectorial TMs were measured for single- and double-pass propagation through step-index MMFs and scattering samples, with corrected phase terms showing agreement across sample types. Furthermore, matrix normality was introduced as a descriptor of stable modal transport. Normal matrices admit unitary diagonalization, reflecting orthogonal eigenchannels and spectrally coherent propagation. Near-normal behavior was observed in fiber TMs, while RMs of scattering slabs remained strongly non-normal, as quantified by a normalized Henrici departure. Sufficient conditions for normality were identified in terms of the system Green's function and its bi-compression onto the measurement basis. A complementary dispersion experiment investigated two regimes: nearly-normal MMFs, where the Wigner–Smith time-delay operator was jointly diagonalizable and supported accurate first-order spectral models; and mechanically compressed fibers, where loss of normality produced noncommuting operators and collapse of model fidelity. These results suggest that normality captures well-behaved modal transport, underpinning the validity of parametric models and other operator-based analyses of disordered media. Together, reciprocity and normality impose complementary constraints on wave transport: reciprocity governs global symmetry, while normality captures internal coherence of modal propagation. Relevance is noted for matrix-based imaging, inverse scattering theory, and non-Hermitian wave physics, where symmetry and modal stability remain central.

Thesis supervisor: Martin Villiger

Title: Assistant Professor of Dermatology

Acknowledgments

I would first like to express my sincere gratitude to my advisor, Prof. Martin Villiger, for his mentorship, guidance, and encouragement throughout the research presented in this thesis. I am also deeply grateful to Dr. Gyeonghun Kim, without whose mentorship and expertise in optics this work would not have been possible. I thank Prof. Brett Bouma for his warm support and advice during the first two years of my doctoral studies. I would also like to thank my friends and colleagues in the Bouma Lab for fostering a friendly and welcoming atmosphere. In particular, I am grateful to Lia Gomez-Perez, Ginger Schmidt, Georgia Jones, Bhaskara Chintada, Sebastián Ruiz-Lopera, Maxina Sheft, Cindy Jie, and Elena Vasquez for their camaraderie, countless discussions, and shared frustrations that made research life far more enjoyable. I also thank Vishal Anantharaman for several fruitful discussions on linear algebra and functional analysis. Finally, I wish to thank my parents, Keshav and Jayshree, my brothers, Tejas and Varchas, and Sahana Prasanna for their unwavering support.

Contents

<i>List of Figures</i>	9
1 Introduction	11
2 Theoretical Framework	17
2.1 Electromagnetic Wave Theory	17
2.1.1 Maxwell's Equations and Electromagnetic Waves	17
2.1.2 Waves in Inhomogeneous Media	20
2.2 Scattering Theory and Mesoscopic Transport	22
2.2.1 The Scattering Matrix	22
2.2.2 Random Matrix Theory of Scattering Matrices	25
2.2.3 Wigner-Smith Time-Delay Operator	26
2.2.4 Measurement of Scattering Matrices	27
2.3 Multimode Fibers	28
2.3.1 Optical Fibers	29
2.3.2 Guided Modes of Multimode Fiber	30
2.3.3 Transmission Matrix of Multimode Fiber	33
2.4 Matrix Analysis and Operator Theory	34
2.4.1 Basic Definitions	35
2.4.2 Eigenvalue and Singular Value Decompositions	35
3 Reciprocity-based Compensation of Aberrations	37
3.1 Aberrations in Optical Systems	37
3.1.1 Origin of Aberrations	37
3.1.2 Correction of Aberrations in Experimental Systems	38
3.2 Reciprocity in Scattering Optics	38
3.3 Methods and Results	40
3.3.1 Measurement of Transmission and Reflection Matrices	40
3.3.2 Correction of Symmetric Operators	42
3.3.3 Correction of Single-Pass MMF TMs	48
4 Normality in Scattering Operators	51
4.1 Normal Matrices	51
4.1.1 Definition and Properties of Normal Matrices	51
4.1.2 Spectra and Pseudospectra of Normal Matrices	51
4.2 Normality of Transmission and Reflection Matrices	53

4.2.1	Green's Function and Stratton-Chu Boundary Field Integrals	53
4.2.2	Operator-Theoretic and Modal Green's Function	54
4.2.3	Compression of the Green's Operator	55
4.2.4	Experimental Analysis of Normality	56
4.2.5	Normality and Parametric Dispersion Modeling	59
5	Discussion and Future Work	65
	<i>References</i>	69

List of Figures

2.1	A schematic of the scattering of an incident wavefront, $U_{\omega}^i(\mathbf{r})$, by an inhomogeneous volume V of some spatially varying refractive index $n(\mathbf{r})$, resulting in a scattered wave $U_{\omega}^s(\mathbf{r})$	20
2.2	Graphical illustration of the scattering system described, based on Fig. 1 in [10]. A disordered slab of length L occupies a region in between waveguides of height D that extend infinitely along the x -axis, supporting infinitely many transverse modes of the form $\sin \frac{n\pi y}{D}$. Any field existing on either side is decomposed into the basis of these supported modes, enabling construction of the scattering matrix as a linear relationship between the mode coefficients of incident and scattered light.	23
2.3	Approach used by S. M. Popoff et al. in [12] to measure the transmission matrix of a disordered slab. A laser operating at 532 nm was used to illuminate a sequence of Hadamard patterns generated using a spatial light modulator onto the sample. The output was imaged onto the CCD array. Complex fields were retrieved using phase-shifting interferometry. Figure taken from [12]. . .	29
2.4	Mode pyramid showing the spatial electromagnetic profiles of the eigenmodes of a step-index multimode fiber. The horizontal m -axis corresponds to the radial mode index, defining the confinement and radial distribution. The vertical l - index defines the azimuthal phase structure and thus the orbital angular momentum of the mode as $\frac{\hbar l}{2}$ per photon. Figure taken from [17]. . .	33
3.1	Pyramid showing the first 21 Zernike polynomials, a set of orthonormal basis functions defined on the unit disk and commonly used for compensation of optical aberrations. Figure taken from Wikipedia [46].	39
3.2	Experimental setup and procedure used in the present investigation to measure transmission and reflection matrices of complex optical media. The sample under examination was scanned with a grid of focal spots, and the output complex field was measured using off-axis holography.	43
3.3	Results of reciprocity-based compensation of double-pass MMF TM (bottom row) and slab RM (top row). (a), (b) composite time-reversal operators $\mathbf{R} \cdot \bar{\mathbf{R}}$ and $\mathbf{T}_{2\times} \cdot \bar{\mathbf{T}}_{2\times}$ before correction (c), (d) Recovered near- and far-field phase profiles for both horizontal (H) and vertical (V) polarizations; (e), (f) Corrected operators after optimization, showing restored symmetry and time-reversibility; (g), (h) Normalized Frobenius norm of the antisymmetric component versus iteration.	46

3.4	Reciprocity-based correction of a single-pass MMF TM. (a) Phase conjugation using the uncorrected single-pass matrix, \mathbf{T}_{fw} , fails to exhibit time-reversibility with the corrected double-pass matrix $\mathbf{T}_{2\times} \cdot (\mathbf{T}_{\text{fw}}^T \cdot \mathbf{T}_{\text{fw}})^\dagger$; (b) Near- and far-field compensatory phase profiles recovered from orthogonal polarization states (H, V) by the proposed method (c) Following optimization, phase conjugation with the corrected single-pass and double-pass operators reconstructs a sharply localized input spot. (d) Convergence of the cosine similarity between the evolving transpose-product $\mathbf{T}_{\text{fw}}^T \cdot \mathbf{T}_{\text{fw}}$ and the target double-pass operator $\mathbf{T}_{2\times}$.	49
4.1	Schur decompositions of single-pass (\mathbf{T}_{fw}), double-pass ($\mathbf{T}_{2\times}$) MMF TMs and eraser RMs (\mathbf{R}). Off diagonal energy decays strongly (select sub-diagonals illustrated by purple, green, and orange lines) for non-normal eraser RM compared to MMF TMs, suggesting mode orthonormality present in structured waveguides like MMF but not general scattering media.	57
4.2	Spectra, pseudospectra, and fields of values of single-pass (\mathbf{T}_{fw}), double-pass ($\mathbf{T}_{2\times}$) MMF TMs and an eraser (\mathbf{R}). The relatively smooth, circular pseudospectral contours of the MMF TMs suggest spectrally stable transport regimes, as opposed to their bloated counterparts in the slab RM.	58
4.3	Effect of fiber normality on first-order dispersion model accuracy. The plot shows cosine similarity with the central TM, \mathbf{T}_8 as a function of wavelength for the MMF msTM. The blue curve represents the uncorrected msTM cosine similarity, while the orange and yellow curves correspond to the first-order dispersion-corrected TMs, $\mathbf{D}(\Delta\omega) \cdot \mathbf{T}_8$, for the unperturbed and mode-scrambled fiber, respectively. Mechanical compression introduced by the fiber-optic mode scrambler reduces the spectral correlation bandwidth of the first-order model, suggesting necessity of higher-order Magnus expansion terms that arise due to non-normality.	62

Chapter 1

Introduction

The propagation of electromagnetic waves in disordered media remains a central topic in modern optics, linking fundamental questions of light–matter interaction with practical applications in imaging, coherent control, telecommunications, and quantum science. In such systems, interference among a large number of spatial and polarization modes gives rise to highly complex transport phenomena that resist simple analytical description. From Maxwell’s equations expressed in the linear, source-free regime, the system’s response to arbitrary excitation is given by convolution with the dyadic Green’s function [1, 2]. However, the Green’s operator is an infinite-dimensional, tensorial operator that relates all points in continuous space to one another, rendering it inaccessible to experimental measurement. To address this complexity, mesoscopic wave transport theory emerged, focusing on statistical characterizations—such as mean free paths and scattering distributions—that describe ensemble properties of photon transport rather than deterministic wave behavior [3–8].

While these statistical treatments provide valuable insights into average behavior, they offer limited guidance for the deterministic control or inversion of specific disordered systems, presenting a bottleneck to exploiting disorder for practical applications. Because the Green’s operator is infinite-dimensional and cannot be directly measured, the scattering matrix formalism offers a practical and experimentally accessible alternative. The scattering matrix provides a finite-dimensional linear mapping between experimentally defined input and output spatial channels [9, 10]. Structurally, the matrix is organized as a block operator, with diagonal blocks corresponding to same-side reflection matrices (RMs) and off-diagonal blocks corresponding to transmission matrices (TMs) in forward and reverse propagation directions [9, 10]. Once measured, the scattering matrix fully characterizes a specific optical system and enables deterministic wavefront control through complex media [10].

While the concept of the scattering matrix as a characterization tool has long been established in wave physics, it was the advent of advanced optical hardware that enabled its practical measurement and application. Spatial light modulators (SLMs) with high pixel counts and fast refresh rates enable precise, dynamic phase-modulation of the input field, while improvements in interferometric detection allow phase-stable, high-resolution measurement of the output wavefront across many spatial modes [10]. Additionally, enhanced system stability, including vibration isolation and thermal regulation has significantly reduced phase noise and drift, making acquisition of complex-valued TMs and RMs matrices feasible in laboratory settings [10].

Building on these advances, Vellekoop and Mosk first demonstrated coherent focusing through a multiply-scattering slab by iteratively optimizing the input wavefront using feedback from output intensity measurements [11]. This seminal experiment provided strong evidence that even highly disordered optical media, previously considered too complex for deterministic control, could be manipulated with precision. Soon after, Popoff et al. introduced a technique for directly measuring the full-field TM of a scattering sample by exciting a Hadamard basis of input fields with a SLM and detecting the transmitted field interferometrically [12]. Using this measured matrix, they demonstrated wavefront shaping via digital phase conjugation and achieved optical focusing through opaque media without iterative optimization. They extended the TM approach to recover a phase image through an opaque sample [13]. Subsequent developments in wavefront shaping further clarified how TMs and RMs could be used for practical control in disordered systems. Popoff et al. demonstrated that time-reversed backscattered fields could be used to focus through aberrating layers onto a few strongly scattering targets, such as gold nanorods, without requiring prior knowledge of their spatial positions [14]. This result underscored the power of operator-based control strategies in opaque and scattering environments, with direct implications for targeted ablation and nonlinear microscopy. Similarly, Ambichl et al. extended the Wigner-Smith time-delay operator, originally developed in quantum mechanics to quantify the dispersion effects of a potential, to optical systems with smoothly varying scattering profiles [15]. Using the spatial derivative of the TM, they demonstrated interior focusing inside scattering media, opening a new class of spatio-temporal control methods based on matrix structure without requiring conjugation optics.

Multimode optical fibers (MMFs) provide an important and increasingly studied platform for matrix-based wavefront control. Although the idealized modal structure of MMFs has been understood for decades, practical implementation of spatial multiplexing has remained challenging due to modal dispersion and intermodal coupling arising from fabrication imperfections, bending, and environmental perturbations [10, 16]. Historically, these limitations led to the perception that MMFs were unsuitable for coherent applications, despite their high spatial channel capacity and theoretical bandwidth. As a result, MMFs have been primarily deployed in short-range datalinks, where modal dispersion is naturally constrained and their adoption is driven more by low manufacturing cost than by spatial complexity. The emergence of wavefront shaping and TM-based techniques has begun to overturn this perception. Plöschner et al. demonstrated that full-field TM measurements can resolve bending-induced mode mixing, polarization effects, and perturbation sensitivity in MMFs, showing that forms of disorder previously regarded as stochastic could be systematically characterized as linear transformations acting on the TM [17]. Complementary work by Carpenter, Eggleton, and Schröder introduced the principal modes of the Wigner–Smith time-delay operator as a natural basis for MMF transport, revealing eigenstates with stability against wavelength tuning and fiber bending [18]. This marked a conceptual shift: from treating MMF output as a random speckle pattern to understanding it as a deterministic, high-dimensional linear transformation governed by underlying modal physics. The robustness of principal modes to spectral perturbations makes them particularly promising for telecommunications, where their wavelength-insensitivity helps mitigate temporal pulse broadening [17]. Matthès et al. extended this line of work by analyzing the stability of MMF transmission under physical deformation [19]. By reconstructing the mode-basis TM, they showed that even in strongly

coupled regimes, the system’s behavior could be described using a small number of deformation parameters. This enabled construction of a reduced set of deformation-invariant modes and highlighted that even in the presence of significant induced disorder, MMF transmission remains amenable to low-dimensional modeling—further supporting the view that MMF TMs are structurally constrained when viewed through an appropriate operator lens.

Deterministic wavefront control and understanding of MMFs is particularly attractive due to their potential as a platform for thin, flexible endoscopes capable of high-resolution imaging. With diameters below 150 μm , MMFs offer an order-of-magnitude reduction in probe size relative to traditional rigid endoscopes, enabling minimally invasive access to delicate anatomical structures. Pioneering work by Čižmár and Dholakia, and independently by Choi et al., demonstrated MMF-based endoscopy by measuring the single-pass TM and using it to invert the scrambled speckle pattern formed at the distal imaging facet [20, 21]. However, a central challenge is that the distal facet, necessary for the single-pass TM calibration, becomes inaccessible once the fiber is inserted into the tissue. Furthermore, even small perturbations—due to bending or temperature drift—disrupt the measured TM and degrade image fidelity. Wen et al. addressed this by introducing a spatial-frequency beacon and a precomputed bank of transmission matrices to compensate for perturbations in real time, integrating their STABLE technique into a clinical-grade white-light endoscope [22]. The investigation by Wen et al. also provides insight into the low-dimensional subspace that governs MMF transmission matrices, suggesting promising avenues for efficient recovery and compensation of these intrinsically high-dimensional operators. However, real-time access to the single-pass MMF TM without distal access remains an outstanding challenge. Proximal recovery strategies have been proposed to circumvent this limitation. Gordon et al. suggested the use of metasurface reflector stacks integrated at the distal facet, enabling reflection-based measurement of the TM [23], and Zheng et al. [24] supplemented it with fast recovery using neural networks. However, these approaches have yet to exploit actual double-pass data experimentally, and the fabrication of such metasurface reflector stacks poses significant practical difficulties. These challenges underscore the need for alternative methods to achieve robust in situ TM recovery.

Beyond endoscopy, TM methods have enabled novel quantum photonic applications using MMFs. Leedumrongwatthanakun et al. demonstrated that MMFs combined with wavefront shaping can serve as reconfigurable linear optical networks, programmable across spatial and polarization modes and validated using two-photon quantum states [25]. Complementing this, Defienne et al. extended the TM concept to nonlinear regimes by implementing a two-photon quantum walk within a MMF supporting hundreds of coupled modes [26]. Their two-photon TM controls multiphoton interference, enabling programmable high-dimensional quantum circuits. These results showcase MMFs as versatile platforms for scalable quantum information processing based on operator-driven control.

Complementary to TM methods in guiding media, reflection matrix (RM) approaches have been developed to address the challenges inherent in deep optical imaging of biological tissues. These media induce aberrations and multiple scattering that degrade image resolution and penetration depth. By measuring the complex RM across a complete set of input channels, it becomes possible to computationally correct for high-order aberrations and multiple scattering effects without the use of fluorescent markers or guide stars [27, 28]. Multi-spectral and time-reversal matrix techniques further extend these capabilities by enabling wavefront correction

across different wavelengths, thereby facilitating volumetric imaging at increased speed and depth [29]. The application of RM-based adaptive optics has demonstrated diffraction-limited imaging through complex barriers, such as the intact mouse skull, indicating the method’s suitability for noninvasive, in vivo imaging with submicron spatial resolution [30]. Furthermore, the principles of matrix imaging have been adapted to other wave phenomena, including ultrasound, where advances in three-dimensional transducer arrays and matrix-based reconstruction have allowed improved aberration correction and image fidelity in complex media [28]. These findings establish RM methods as an extensible approach for the characterization and control of propagation in scattering environments, with implications extending from wave physics to biomedical imaging.

Although TM and RM-based techniques are now applied across imaging, communications, and quantum optics, the underlying operator structure of the SM itself has received comparatively little scrutiny. Most implementations treat the matrix as a numerical object to be optimized or inverted, relying on imaging heuristics or black-box algorithms rather than on a rigorous analysis of its mathematical properties. Apart from random-matrix studies of ensemble-averaged singular-value statistics [cite], few works examine how a measured TM or RM should behave in a real, deterministic system. A first and natural constraint is reciprocity: first articulated by Helmholtz [31–33] and later extended to all harmonic wave systems by Lord Rayleigh [34, 35], source–observer interchangeability implies that the full scattering matrix is transpose-symmetric, yielding symmetric RM blocks and mutually transposed forward and reverse TM blocks [9, 10]. Even when a sample’s TM or RM may obey reciprocity-induced constraints, typical measurements can violate them in two ways: (1) by using distinct illumination and detection paths, which break the exchange symmetry without contravening the underlying physics; and (2) by incorporating components like circulators, which break reciprocity at a physical level by introducing magneto-optic or active effects. Knowledge of reciprocity-induced symmetries thus affords a way to distinguish scattering within a medium from distortions introduced by the measurement apparatus. This thesis develops a matrix-based optimization procedure that enforces reciprocity, recovering the physically admissible TM or RM and isolating the corresponding system-level phase corrections. Familiar experimental aberrations, such as tilt, emerge naturally as violations of reciprocity-induced symmetry, rather than explicit parametric modeling.

Furthermore, normality—defined as commutation of a matrix with its adjoint [36]—is proposed as a mathematical lens under which to study the stability and perturbation response of complex optical media. Normal operators admit diagonalization by a unitary operator [36] and hence support an orthogonal set of eigenchannels, corresponding to stable, invertible transport. Normality relaxes the constraint of unitarity, which imposes a strict condition of unit-magnitude eigenvalues, allowing potentially lossy but decoupled eigenmodes of propagation in wave systems [36]. This thesis investigates the role of matrix normality in differentiating carefully engineered optical waveguides, like MMF, from general disordered media. It is shown that under appropriate spatial sampling, the single- and double-pass TMs of MMF exhibit high normality, quantified using a modified form of Henrici’s departure [37]. On the other hand, RMs from a scattering slab remain highly non-normal despite accurate spatial registration. Conditions for inheritance of normality from the underlying Green’s operator is given with respect to operator compression.

The remainder of this thesis is organized as follows. Chapter 2 covers selected background

material in electromagnetic wave theory, scattering optics, mesoscopic transport, multimode fiber physics, and matrix analysis, relevant for complete understanding of the work presented. Chapter 3 introduces the proposed reciprocity-based compensation of aberrations. Chapter 4 covers the investigation on matrix normality in scattering media. Chapter 5 contains discussion, conclusions and potential future directions for the work presented.

Chapter 2

Theoretical Framework

2.1 Electromagnetic Wave Theory

2.1.1 Maxwell's Equations and Electromagnetic Waves

The propagation of electromagnetic waves in dielectric media is governed by Maxwell's equations [9]:

$$\nabla \cdot \epsilon_0 \mathbf{E} = -\nabla \cdot \mathbf{P} + \rho \quad (2.1)$$

$$\nabla \cdot \mu_0 \mathbf{H} = -\nabla \cdot \mu_0 \mathbf{M} \quad (2.2)$$

$$\nabla \times \mathbf{E} = -\frac{\partial}{\partial t} \mu_0 \mathbf{H} - \frac{\partial}{\partial t} \mu_0 \mathbf{M} \quad (2.3)$$

$$\nabla \times \mathbf{H} = \frac{\partial}{\partial t} \epsilon_0 \mathbf{E} + \frac{\partial}{\partial t} \mathbf{P} + \mathbf{J}, \quad (2.4)$$

where \mathbf{E} is the electric field, \mathbf{P} is the polarization density of the medium, \mathbf{M} is the magnetization density of the medium, \mathbf{H} is the magnetic field, and \mathbf{J} is the current density. The fundamental constants μ_0 and ϵ_0 are the free space magnetic permeability and electric permittivity [9]. In linear, isotropic, dispersionless media, the electric and magnetic polarizations of the medium, corresponding to medium response, are linearly related to the applied electric and magnetic fields, respectively:

$$\mathbf{P} = \epsilon_0 \chi_e \mathbf{E} \quad (2.5)$$

$$\mathbf{M} = \chi_m \mathbf{H}, \quad (2.6)$$

where the χ_e and χ_m are the scalar electric and magnetic susceptibilities, respectively [9]. The dielectric constant of the medium $\epsilon \equiv \epsilon_0(1 + \chi_e)$ and $\mu = \mu_0(1 + \chi_m)$. In the case of a source-free medium, where there are no external charges or currents, $\mathbf{J} = 0$ and $\rho = 0$. Taking the curl of Faraday's law, the third of Maxwell's equations, yields [9]:

$$\nabla \times (\nabla \times \mathbf{E}) = -\mu\epsilon \frac{\partial \mathbf{E}}{\partial t}. \quad (2.7)$$

For a twice-differentiable vector field \mathbf{A} , $\nabla \times \nabla \times \mathbf{A} = \nabla(\nabla \cdot \mathbf{A}) - \nabla^2 \mathbf{A}$. Hence, a wave equation emerges if $\nabla \cdot \mathbf{E} = 0$:

$$\nabla^2 \mathbf{E} = \mu \epsilon \frac{\partial^2}{\partial t^2} \mathbf{E}. \quad (2.8)$$

The general solutions for \mathbf{E} and \mathbf{H} must satisfy both Eq. 2.8 as well as the constraints imposed by Maxwell's equations.

Since Maxwell's equations are linear differential equations, a sinusoidal excitation at a given frequency results in oscillation of the electromagnetic field at the same frequency [9]. It is therefore natural to consider time-harmonic eigenfunctions of the Maxwell operator, $\mathbf{E} \equiv \mathbf{E}(\mathbf{r})e^{j\omega t}$, $\mathbf{H} \equiv \mathbf{H}(\mathbf{r})e^{j\omega t}$, and $\mathbf{J} \equiv \mathbf{J}(\mathbf{r})e^{j\omega t}$, in which the dependence on the spatial variable \mathbf{r} has been separated from the temporal oscillation described by $e^{j\omega t}$. Under this ansatz, temporal derivatives $\frac{\partial}{\partial t}$ reduce to multiplication by $j\omega$, and Maxwell's equations simplify to differential equations in the spatial variable only:

$$\nabla \cdot \epsilon_0 \mathbf{E} = \rho \quad (2.9)$$

$$\nabla \cdot \mu_0 \mathbf{H} = 0 \quad (2.10)$$

$$\nabla \times \mathbf{E} = -j\omega \mu \mathbf{H} \quad (2.11)$$

$$\nabla \times \mathbf{H} = j\omega \epsilon \mathbf{E} + \mathbf{J}. \quad (2.12)$$

The corresponding wave equation, which results from applying the assumption of these time-harmonic fields to Eq. 2.8, is called the vectorial Helmholtz equation [9, 10]:

$$\mathcal{L} \mathbf{E}_\omega \equiv \left(\nabla^2 + \frac{\omega^2}{c^2} \epsilon(\mathbf{r}) \right) \mathbf{E}_\omega(\mathbf{r}) = \mathbf{0}, \quad (2.13)$$

where the linear differential operator $\mathcal{L} \equiv \nabla^2 + \frac{\omega^2}{c^2} \epsilon(\mathbf{r})$. Fundamental plane waves traveling along the direction of the wavevector $\mathbf{k} = \frac{\omega}{c} \hat{\mathbf{k}}$ are solutions for the electric and magnetic fields [9]:

$$\mathbf{E}(\mathbf{r}, t) = \mathbf{E} e^{-j\mathbf{k} \cdot \mathbf{r}} \quad (2.14)$$

$$\mathbf{H}(\mathbf{r}, t) = \mathbf{H} e^{-j\mathbf{k} \cdot \mathbf{r}}, \quad (2.15)$$

where \mathbf{E} and \mathbf{H} are complex amplitudes of the fields that are orthogonal to the propagation direction of the wave, i.e., $\mathbf{k} \cdot \mathbf{E} = \mathbf{k} \cdot \mathbf{H} = 0$.

The harmonic Maxwell equations exhibit several symmetries worth mentioning. Suppose two independent sets of field solutions, $(\mathbf{E}_a, \mathbf{H}_a)$ and $(\mathbf{E}_b, \mathbf{H}_b)$, are given, such that

$$\nabla \times \mathbf{E}_a = -j\omega \mu \mathbf{H}_a \quad (2.16)$$

$$\nabla \times \mathbf{H}_a = j\omega \epsilon \mathbf{E}_a \quad (2.17)$$

and

$$\nabla \times \mathbf{E}_b = -j\omega \mu \mathbf{H}_b \quad (2.18)$$

$$\nabla \times \mathbf{H}_b = j\omega \epsilon \mathbf{E}_b. \quad (2.19)$$

Dot-multiplying Eq. 2.16 by \mathbf{H}_b , Eq. 2.17 by \mathbf{E}_b , and summing yields

$$(\nabla \times \mathbf{E}_a) \cdot \mathbf{H}_b + (\nabla \times \mathbf{H}_a) \cdot \mathbf{E}_b = -j\omega[\mu\mathbf{H}_b \cdot \mathbf{H}_a - \epsilon\mathbf{E}_b \cdot \mathbf{E}_a]. \quad (2.20)$$

A similar equation, with subscripts interchanged, can be constructed by dot-multiplying Eq. 2.18 by \mathbf{H}_a , Eq. 2.19 by \mathbf{E}_a , and summing:

$$(\nabla \times \mathbf{E}_b) \cdot \mathbf{H}_a + (\nabla \times \mathbf{H}_b) \cdot \mathbf{E}_a = -j\omega[\mu\mathbf{H}_a \cdot \mathbf{H}_b - \epsilon\mathbf{E}_a \cdot \mathbf{E}_b]. \quad (2.21)$$

Subtracting Eq. 2.21 from 2.20 and noting that for differentiable vector fields \mathbf{A}, \mathbf{B} : $\nabla \cdot (\mathbf{A} \times \mathbf{B}) = (\nabla \times \mathbf{A}) \cdot \mathbf{B} - \mathbf{A} \cdot (\nabla \times \mathbf{B})$,

$$\nabla \cdot (\mathbf{E}_a \times \mathbf{H}_b - \mathbf{E}_b \times \mathbf{H}_a) = 0, \quad (2.22)$$

where the right-hand sides have canceled due to commutativity of the dot product operation. Integrating over a volume V that encloses a and b , and applying the divergence theorem to convert the volume integral to a surface integral over $S = \partial V$ yields

$$\oint_S (\mathbf{E}_a \times \mathbf{H}_b) \cdot d\mathbf{A} = \oint_S (\mathbf{E}_b \times \mathbf{H}_a) \cdot d\mathbf{A}. \quad (2.23)$$

This is known as the Lorentz reciprocity theorem [9]. Conceptually, Eq. 2.23 can be interpreted as follows: the quantities $\mathbf{E}_a \times \mathbf{H}_b$ and $\mathbf{E}_b \times \mathbf{H}_a$ correspond to the mutual coupling between the field solutions at a and b . The volume (or equivalently, surface) integral captures the net "flux" between the two field solutions in space. In reciprocal media, this relationship is symmetric: the net flux associated with $(\mathbf{E}_a, \mathbf{H}_a)$ in the presence of $(\mathbf{E}_b, \mathbf{H}_b)$ is equal to the net flux associated with $(\mathbf{E}_b, \mathbf{H}_b)$ in the presence of $(\mathbf{E}_a, \mathbf{H}_a)$. In other words, reciprocity is the electromagnetic statement that mutual coupling is fundamentally symmetric.

A related concept is time-reversal symmetry. The equations (2.13) and (2.14) remain unchanged under complex conjugation, with new field solutions $\overline{\mathbf{E}}$ and $-\overline{\mathbf{H}}$. As a result, a plane wave traveling in the $+z$ propagation direction with evolution $\exp j\beta z$ is converted to one with evolution given by $\exp -j\beta z$ [9]. The new wave travels backwards in time (or space) with a conjugated field phasor [9]. Though reciprocity holds for all linear, source-free systems, strict time-reversal symmetry holds only for lossless media, because the wave must be traced back in time and space without attenuation [9]; though, in practice, approximate retracing of the wavefront is still often possible [10, 12, 13]. Thus, time-reversal symmetry implies reciprocity, but reciprocity does not necessarily imply strict time-reversal symmetry [9, 10]

Due to the difficulty in analytically solving the vectorial form of the Helmholtz equation in most practical cases, the scalar Helmholtz equation is a useful approximation, assuming that vectorial components do not mutually couple [9, 10]. Here, the vectorial electric field is approximated as acting primarily along one direction such that $\mathbf{E}_\omega(\mathbf{r}) \approx \psi_\omega(\mathbf{r})$. This allows decoupling of spatial and polarization variation:

$$\left(\nabla^2 + \frac{\omega^2}{c^2} \epsilon(\mathbf{r}) \right) \psi_\omega(\mathbf{r}) = 0. \quad (2.24)$$

While the homogeneous form describes freely propagating or resonant fields, most physical scenarios involve sources or scatterers that introduce inhomogeneity. To account for these, one must turn to the inhomogeneous Helmholtz equation, whose solution naturally involves the use of Green's functions [2, 10].

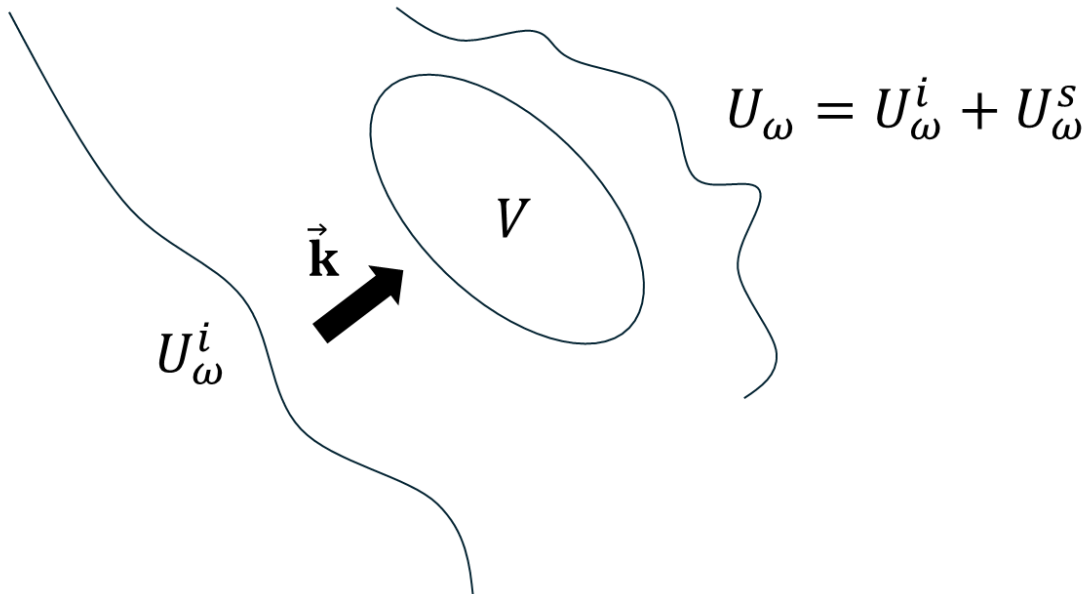


Figure 2.1: A schematic of the scattering of an incident wavefront, $U_\omega^i(\mathbf{r})$, by an inhomogeneous volume V of some spatially varying refractive index $n(\mathbf{r})$, resulting in a scattered wave $U_\omega^s(\mathbf{r})$.

2.1.2 Waves in Inhomogeneous Media

Having established the behavior of electromagnetic waves in free space, it is natural to ask how such waves are modified upon encountering matter. Since Maxwell's equations must be satisfied in all space, the presence of a material medium imposes boundary conditions and spatial variations that alter the wave's structure. This question motivates the framework of scattering theory, which provides a systematic approach to describing how incident fields are transformed by their interaction with dielectric media. In the scalar formulation presented here, the case of a monochromatic electromagnetic wave incident on an isotropic, non-magnetic, source-free medium occupying some finite volume V is considered. The treatment closely follows Chapter 13 of [1], to which the reader is referred for a full vectorial treatment and further physical applications. The electric field must at all points satisfy the vector Helmholtz equation in all of space:

$$\nabla^2 \mathbf{E}_\omega(\mathbf{r}) + k^2 n_\omega^2(\mathbf{r}) \mathbf{E}_\omega(\mathbf{r}) = 0. \quad (2.25)$$

In the scalar case, coupling between different components of $\mathbf{E}_\omega(\mathbf{r})$ is considered negligible. Denoting by $U_\omega(\mathbf{r})$ a single Cartesian component of $\mathbf{E}_\omega(\mathbf{r})$, the starting point of the analysis begins from the equation:

$$\nabla^2 U_\omega(\mathbf{r}) + k^2 n_\omega^2(\mathbf{r}) U_\omega(\mathbf{r}) = 0. \quad (2.26)$$

It is convenient to rewrite Eq. (2.21) as:

$$\nabla^2 U_\omega(\mathbf{r}) + k^2 U_\omega(\mathbf{r}) = -4\pi F_\omega(\mathbf{r}) U_\omega(\mathbf{r}), \quad (2.27)$$

where

$$F_\omega(\mathbf{r}) = \frac{1}{4\pi} k^2 (n_\omega^2(\mathbf{r}) - 1). \quad (2.28)$$

F is called the scattering potential of the medium, in analogy with the terminology used in quantum field theory when discussing scattering of a non-relativistic particle obeying the time-independent Schrodinger equation.

The analysis proceeds by considering the total field, $U_\omega(\mathbf{r})$ to be a sum of the incident field, $U_\omega^i(\mathbf{r})$, and the scattered field, $U_\omega^s(\mathbf{r})$ (Fig. 2.1):

$$U_\omega(\mathbf{r}) = U_\omega^i(\mathbf{r}) + U_\omega^s(\mathbf{r}). \quad (2.29)$$

Since the incident field is assumed to be a plane wave, it obeys the scalar Helmholtz equation,

$$(\nabla^2 + k^2)U_\omega^i(\mathbf{r}) = 0, \quad (2.30)$$

in all of space. The scattered field must then obey the equation

$$\nabla^2 U_\omega^s(\mathbf{r}) + k^2 U_\omega^s(\mathbf{r}) = -4\pi F_\omega(\mathbf{r}) U_\omega(\mathbf{r}). \quad (2.31)$$

Since the scalar Helmholtz equation is a linear differential equation, its solution can be expressed in integral form by considering the Green's function $G_\omega(\mathbf{r} - \mathbf{r}')$, which satisfies

$$(\nabla^2 + k^2)G_\omega(\mathbf{r} - \mathbf{r}') = -4\pi\delta_\omega^3(\mathbf{r} - \mathbf{r}'), \quad (2.32)$$

where $\delta_\omega^3(\mathbf{r} - \mathbf{r}')$ is the three-dimensional Dirac delta function. The only assumption made is that G_ω is symmetric, i.e., $G_\omega(\mathbf{r}, \mathbf{r}') = G_\omega(\mathbf{r}', \mathbf{r})$.

Here, since G_ω itself describes a valid solution to the Helmholtz operator, it may encapsulate the complete response of the system, permitting the scattering potential to be taken as identically zero. Conversely, one may adopt the free-space Green's function and represent all inhomogeneities within the scattering potential. Thus, the division between Green's function and potential is a matter of formal convenience, rather than a physical necessity, and the total response of the medium is equivalently described in either representation. This flexibility allows the analyst to choose a Green's function that simplifies either numerical implementation or analytical treatment, without altering the physical content of the solution. In conventional scattering theory of free space with discrete scatterers, it is often convenient to adopt the free-space Green's function and encode all inhomogeneities within the scattering potential, as this explicitly isolates the contribution of each scatterer. In contrast, for structured systems such as waveguides or multimode fibers, the Green's function is frequently chosen to satisfy the boundary conditions of the system, thereby capturing the effects of geometry and confinement, and the scattering potential is often unnecessary or even omitted in practice.

This distinction in the choice of Green's function naturally informs the integral representation of the scattered field. Whether the Green's function encapsulates the full system response or the inhomogeneities are encoded in a separate scattering potential, the scattered field may always be expressed as an integral over the volume of the perturbation and the bounding surface, with the Green's function mediating the interaction. In this manner, the

formalism unifies both approaches, and the subsequent expression for U_ω^s holds irrespective of the specific partitioning between Green's function and scattering potential. After some manipulations, it is found that the scattered field may be expressed using G_ω as:

$$U_\omega^s(\mathbf{r}) = \int_V F_\omega(\mathbf{r}')U_\omega(\mathbf{r}')G_\omega(\mathbf{r} - \mathbf{r}') d^3r' - \frac{1}{4\pi} \int_{S_R} \left[U_\omega^s(\mathbf{r}') \frac{\partial G_\omega(\mathbf{r} - \mathbf{r}')}{\partial n'} - G_\omega(\mathbf{r} - \mathbf{r}') \frac{\partial U_\omega^s(\mathbf{r}')}{\partial n'} \right] dS_R, \quad (2.33)$$

where integration is performed over the volume of the scatterer V enclosed by a large sphere S_R of radius R , and $\frac{\partial}{\partial n'}$ denotes differentiation along the outward normal unit vector \mathbf{n}' to the surface of S_R . Thus far, the only assumption made about the Green's function is that it is symmetric and satisfies the scalar Helmholtz equation. Choosing, as an example, the free-space Green's function of the form

$$G_\omega(\mathbf{r} - \mathbf{r}') = \frac{e^{jk|\mathbf{r}-\mathbf{r}'|}}{|\mathbf{r} - \mathbf{r}'|}, \quad (2.34)$$

Eq. (2.28) reduces to

$$U_\omega^s(\mathbf{r}) = \int_V F_\omega(\mathbf{r}')U_\omega(\mathbf{r}') \frac{e^{jk|\mathbf{r}-\mathbf{r}'|}}{|\mathbf{r} - \mathbf{r}'|} d^3r. \quad (2.35)$$

The total field is then expressed as

$$U_\omega(\mathbf{r}) = U_\omega^i(\mathbf{r}) + \int_V F_\omega(\mathbf{r}')U_\omega(\mathbf{r}') \frac{e^{jk|\mathbf{r}-\mathbf{r}'|}}{|\mathbf{r} - \mathbf{r}'|} d^3r, \quad (2.36)$$

In such cases where closed-form solutions to Eq. (2.31) are intractable, especially for complex or disordered media, alternative formulations become necessary. One approach is to shift from solving the field equations directly to describing how the medium transforms incoming waves into outgoing waves. This perspective abstracts the problem to input-output relations rather than full spatial field distributions. The next section introduces this framework more formally.

2.2 Scattering Theory and Mesoscopic Transport

2.2.1 The Scattering Matrix

The Green's function formalism provides a complete description of how waves propagate through a medium in response to refractive index inhomogeneities. However, in many practical scenarios, especially in structured or bounded systems, modeling the full vectorial scattering integral for arbitrary refractive index distributions becomes impractical. Thus, rather than solving for fields throughout continuous space, one asks: how does a wave entering the system in a given channel emerge after interacting with the medium? Under the assumption of a linear system under examination, this leads naturally to the framework of scattering theory,

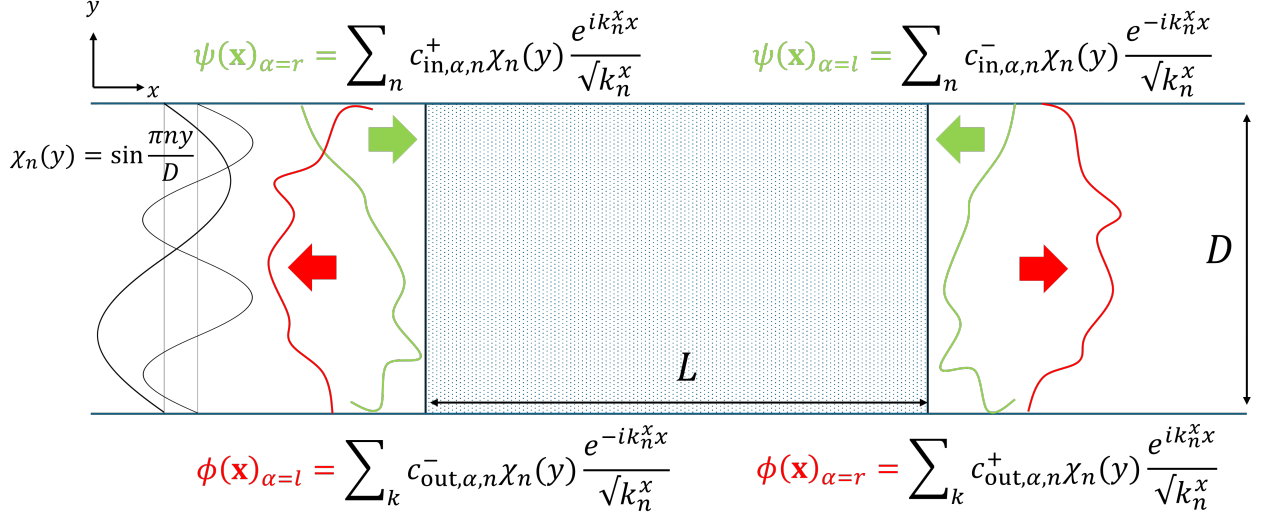


Figure 2.2: Graphical illustration of the scattering system described, based on Fig. 1 in [10]. A disordered slab of length L occupies a region in between waveguides of height D that extend infinitely along the x -axis, supporting infinitely many transverse modes of the form $\sin \frac{n\pi y}{D}$. Any field existing on either side is decomposed into the basis of these supported modes, enabling construction of the scattering matrix as a linear relationship between the mode coefficients of incident and scattered light.

where the central object is the scattering matrix, or \mathbf{S} -matrix, which encodes how each input mode is reflected or transmitted into output modes.

The approach developed here closely follows the framework discussed in [10], and models wave scattering through a general disordered medium. The medium is embedded between two infinitely extended slab waveguides, each supporting a discrete set of sinusoidal resonant modes. The disordered region shares the same height as the waveguides, and the system is enclosed by Dirichlet boundary conditions, which confine the waves within the structure. The system under examination is shown in Fig. 2.2. This example, while not an explicit description of any particular experimental setup, illustrates the conceptual motivation for scattering matrices and modal structure used throughout the present thesis. The slab waveguides on either side of the disordered medium support a discrete set of transverse modes, corresponding to sinusoidal field distributions whose wavelengths satisfy resonance conditions imposed by the waveguide boundaries. Therefore, the guided portion of any field in these waveguides is decomposed into the basis of non-evanescent modes, whose evanescent counterparts are assumed to have died out asymptotically.

The mode of order n supported by the waveguides on either side of the slab is:

$$\chi_n = \sqrt{\frac{2}{D}} \sin\left(\frac{n\pi y}{D}\right). \quad (2.37)$$

Consider an arbitrary field $\psi(\mathbf{x})$ incident on the disordered medium. It can be written as a superposition of modes with coefficients c_{in}^+ and c_{in}^- corresponding to right ($\alpha = r$) and left

($\alpha = l$) traveling waves, respectively:

$$\psi(\mathbf{x}) = \sum_{n=1}^N c_{\text{in}, \alpha, n}^+ \chi_n(y) \frac{e^{ik_n^x x}}{\sqrt{k_n^x}} + c_{\text{in}, \alpha, n}^- \chi_n(y) \frac{e^{-ik_n^x x}}{\sqrt{k_n^x}}, \quad (2.38)$$

where N is chosen arbitrarily to bound the support of the system. The field scattered by the medium, denoted $\phi(\mathbf{x})$, is coupled into the same waveguide modes as the incident field with coefficients c_{out}^+ , c_{out}^- determined by the scattering process:

$$\phi(\mathbf{x}) = \sum_{n=1}^N c_{\text{out}, \alpha, n}^+ \chi_n(y) \frac{e^{ik_n^x x}}{\sqrt{k_n^x}} + c_{\text{out}, \alpha, n}^- \chi_n(y) \frac{e^{-ik_n^x x}}{\sqrt{k_n^x}}. \quad (2.39)$$

Then, the linear input-output relationship between the set of input and output expansion coefficients in each of the energy-carrying modes, denoted \mathbf{c}_{in} and \mathbf{c}_{out} , respectively, can be collected in the scattering matrix:

$$\mathbf{c}_{\text{in}} = \mathbf{S} \cdot \mathbf{c}_{\text{out}}, \quad (2.40)$$

where the incoming modes from the left and right, \mathbf{c}_i , are connected to the resulting outgoing left- and right-modes such that \mathbf{S} is of size $2N \times 2N$. \mathbf{S} can therefore be subdivided into same-side reflection blocks (\mathbf{r}, \mathbf{r}') and opposite side transmission blocks (\mathbf{t}, \mathbf{t}'):

$$\mathbf{S} = \begin{bmatrix} \mathbf{r} & \mathbf{t}' \\ \mathbf{t} & \mathbf{r}' \end{bmatrix}, \quad (2.41)$$

Reciprocity ensures that exchanging the roles of source and observer leaves the system's response unchanged. This corresponds to transpose symmetry of the scattering matrix, $\mathbf{S} = \mathbf{S}^T$, meaning that the amplitude and phase relationship between any two modes is the same in either direction of scattering [9, 10]. Hence $\mathbf{r} = \mathbf{r}^T$, $\mathbf{r}' = \mathbf{r}'^T$, and $\mathbf{t}' = \mathbf{t}^T$. If the medium is assumed to be without gain or loss, energy conservation may be imposed by equating the total input and output energy:

$$\mathbf{c}_{\text{out}}^\dagger \cdot \mathbf{c}_{\text{out}} = \mathbf{c}_{\text{in}}^\dagger \cdot \mathbf{c}_{\text{in}}. \quad (2.42)$$

Since $\mathbf{c}_{\text{in}} = \mathbf{S} \cdot \mathbf{c}_{\text{out}}$, this simplifies to:

$$\mathbf{c}_{\text{in}}^\dagger \cdot (\mathbf{S}^\dagger \mathbf{S} - \mathbf{I}) \cdot \mathbf{c}_{\text{in}} = 0, \quad (2.43)$$

from which it follows that $\mathbf{S}^\dagger \mathbf{S} = \mathbf{I}$, i.e., \mathbf{S} is unitary [10]. Therefore, it supports a basis of orthonormal eigenmodes:

$$\mathbf{S} = \mathbf{P} \cdot \mathbf{\Lambda} \cdot \mathbf{P}^\dagger, \quad (2.44)$$

where the columns of \mathbf{P} contain the orthonormal eigenvectors of \mathbf{S} and $\mathbf{\Lambda}$ is a diagonal matrix with unit-norm eigenvalues known as scattering phase shifts. Conceptually, this means that the modes of \mathbf{S} undergo phase-only transformation upon scattering by the medium.

If the unitary condition of \mathbf{S} is expanded to consider the transmission and reflection components, it is found that [10]:

$$\mathbf{t}^\dagger \mathbf{t} + \mathbf{r}^\dagger \mathbf{r} = \mathbf{t}'^\dagger \mathbf{t}' + \mathbf{r}'^\dagger \mathbf{r}' = \mathbf{1} \quad (2.45)$$

$$\mathbf{r}^\dagger \mathbf{t}' + \mathbf{t}^\dagger \mathbf{r}' = \mathbf{t}'^\dagger \mathbf{r} + \mathbf{r}'^\dagger \mathbf{t} = \mathbf{0}. \quad (2.46)$$

A common assumption in mostly lossless systems, such as optical fibers or integrated photonic waveguides, is that reflection is negligible due to good index matching or minimal mode mismatch at interfaces. Under this assumption, $\mathbf{S} \approx \mathbf{T}$ and \mathbf{T} is approximately unitary. This assumption is particularly valid in systems with long propagation lengths and low numerical aperture (NA), where scattering is weak and forward-propagating modes dominate. However, while unitarity guarantees orthonormal eigenchannels and energy conservation in idealized, closed, or reflectionless systems, it is often too strict to describe realistic photonic media. Most systems, especially those involving mode mismatch, partial reflections, or lossy boundaries, break unitarity without becoming disordered or pathological. Moreover, the unitary condition is often invoked as a direct consequence of energy conservation, but this connection is largely heuristic and lacks a rigorous spectral foundation, an oversight that obscures the deeper structure governing mode behavior in near-conservative systems. It is this gap that motivated the investigation of normality, which is covered in more detail in later sections of this thesis.

2.2.2 Random Matrix Theory of Scattering Matrices

Having thus established the formal structure by which the propagation of waves in multimode systems may be described, through the decomposition of fields into orthogonal modal components and their evolution governed by transmission and reflection matrices, it becomes natural to inquire not only into the precise behavior of individual systems, but also into the statistical character of such behavior when subjected to perturbations or disorder. This analysis follows closely the one presented in [10]. In such settings, where the precise details of the medium are either unknown or too complex to model directly, a deterministic description gives way to one of statistical regularity [10]. It was in this spirit that the methods of random matrix theory were first introduced, initially in the context of nuclear scattering by Wigner [38], and later adapted to describe the transport of electrons in disordered conductors [3]. More recently, similar techniques have found application in the analysis of wave propagation in optical systems [10], where the formal parallels to quantum transport are particularly strong [3, 10]. Within this framework, the transmission and scattering matrices are no longer treated as fixed operators, but rather as elements of suitable statistical ensembles, constrained by fundamental symmetries such as energy conservation, reciprocity, and time-reversal invariance. The intent is not to predict a specific outcome, but to characterize the distribution of possible outcomes that may arise under well-defined physical assumptions.

The approach originally considered by Wigner and Dyson [38, 39] chooses each of the elements of a system's Hamiltonian \mathbf{H}_{mn} from a family of Gaussian ensembles whose probability distribution is given by $P(\mathbf{H}_{mn}) = \frac{1}{w\sqrt{2\pi}} \exp \frac{-\mathbf{H}_{mn}^2}{2w^2}$ with zero mean $\langle \mathbf{H}_{mn} \rangle = 0$ where the parameter w controls the spacing between the eigenvalues of \mathbf{H} . It can be shown that

the eigenvalues of these matrices follow the distribution

$$P(\{E_n\}) \propto \prod_{m < n}^N |E_n - E_m|^\beta \prod_n^N \exp\left(\frac{-E_n^2}{2w^2}\right), \quad (2.47)$$

where the parameter $\beta = 1$ for the Gaussian orthogonal ensemble (GOE) and $\beta = 2$ for the Gaussian unitary ensemble, corresponding to the distributions from which \mathbf{H} is sampled, and E_i are the eigenvalues of \mathbf{H} . A similar formalism exists when considering directly the elements of the scattering matrix in lieu of the system Hamiltonian, which must obey unitarity and transpose-symmetry [10]. Analogously, each element is chosen as a random complex number and the scattering matrix must obey the unitarity and transpose-symmetry conditions [10]. The ensemble of such matrices has an eigenvalue distribution, corresponding to the scattering phase shifts ϕ , known as the Dyson circular ensemble [10, 39]:

$$P(\{\phi_n\}) = \prod_{n < m} |\exp(i\phi_n) - \exp(i\phi_m)|^\beta. \quad (2.48)$$

And for the TM, \mathbf{t} , the transmission eigenchannel distribution is given by [10, 40]:

$$P(\{\tau_n\}) \propto \prod_{m < b} |\tau_n - \tau_m|^\beta \times \prod_p \tau_p^{\frac{\beta}{2}-1}. \quad (2.49)$$

In the limit of a large number of scattering channels, this distribution follows

$$P(\tau) = \frac{1}{\pi\sqrt{\tau(1-\tau)}}, \quad (2.50)$$

where τ are the real-valued eigenvalues of the Hermitian matrix $\mathbf{t}^\dagger \mathbf{t}$ that correspond to channels of maximum energy transmission [10]. The function $P(\tau)$ approaches very high values asymptotically for $\tau \rightarrow 0$ or $\tau \rightarrow 1$. This is not an intuitive result: it says that eigenchannels of even highly disordered media, in the statistical sense, are either fully transmitting or fully attenuating.

While the insights of random matrix theory capture universal features that transcend specific system details, they are inherently statistical: they describe what is typical or likely across an ensemble, not what occurs in any particular instance. As such, their utility is limited when one wishes to manipulate, or control the behavior of a specific physical system, such as a real optical fiber with known geometry, fabrication imperfections, or environmental influences. The remainder of this thesis departs from this foray into ensemble-averaged descriptions and turns instead back to characterization of specific optical systems. The interested reader is directed to [3] for a thorough coverage of this topic.

2.2.3 Wigner-Smith Time-Delay Operator

In systems governed by coherent linear scattering, the frequency dependence of the scattering matrix encodes valuable dynamical information. In particular, the question of how long a wave packet is delayed by passage through a potential or scattering region has motivated

formal developments across quantum and optical physics. A rigorous approach to this problem was introduced by Eugene Wigner in quantum mechanics, who sought to define a meaningful delay time associated with the scattering of a wave packet from a localized potential [38]. His work was later extended by Felix Smith, who introduced a matrix formulation to account for scattering in systems with more than one open channel [41].

Consider a linear, source-free optical system, in which responses to an input field are governed by frequency-dependent unitary scattering operator, $\mathbf{S}(\omega)$:

$$\vec{y} = \mathbf{S}(\omega)\vec{x}. \quad (2.51)$$

The frequency derivative operator of the system response can be written as:

$$\partial_\omega \equiv \frac{\partial \mathbf{S}}{\partial \omega} \mathbf{S}^{-1}. \quad (2.52)$$

The instantaneous dispersion matrix ∂_ω describes the phase shift of output modes with respect to a frequency change. This motivates the definition of the Wigner-Smith time-delay operator, which instead captures the instantaneous phase change of the input modes due to a frequency shift [41, 42]:

$$\mathbf{Q} = -j \mathbf{S}^{-1} \cdot \frac{\partial \mathbf{S}}{\partial \omega} \quad (2.53)$$

$$\equiv -j \mathbf{S}^\dagger \cdot \frac{\partial \mathbf{S}}{\partial \omega}, \quad (2.54)$$

where the multiplication by $-j$ serves to make the anti-Hermitian matrix $\frac{\partial \mathbf{S}}{\partial \omega}$ Hermitian, to ensure real eigenvalues necessary for physically observable mode dwell times. The concept of the Wigner-Smith operator has also been applied to more general perturbations, including spatial and structural changes in complex media [15, 19]. Its eigenstates are increasingly studied in broadband and time-sensitive applications, such as time-resolved imaging and ultrafast communications [18]. They also provide insight into the modal structure of delay in complex systems.

2.2.4 Measurement of Scattering Matrices

While the scattering matrix (SM) provides a complete linear mapping between incoming and outgoing electromagnetic fields, it is fundamentally defined over infinite-dimensional Hilbert spaces. A “true” SM would require the ability to synthesize arbitrary input fields and to detect the full complex vector field across all output channels. This is physically unrealizable in any experimental setting, particularly in complex media where light is multiply scattered and energy may be redistributed into inaccessible spatial or polarization channels.

To make the SM experimentally accessible, one instead measures its projection onto a finite-dimensional subspace of controllable and observable modes. A widely adopted approach, introduced by Popoff et al. (2010) [12], achieves this using spatial light modulators (SLMs) to encode known input phase patterns and off-axis holography or phase-shifting interferometry

to recover the complex-valued output fields, as shown in Fig. 2.3. In a typical setup, a collimated laser beam is shaped by a SLM to generate a prescribed input wavefront, which illuminates the sample. The resulting scattered field is then interfered with a coherent reference beam on a camera, allowing recovery of both amplitude and phase. To ensure phase consistency across input modes, global interferometric drift is corrected either actively, using embedded reference modes, or by rephasing each measurement relative to a common reference mode.

The measurement proceeds by scanning through a complete input basis—such as Hadamard patterns, pixel-wise delta functions, or low-order spatial harmonics—and assembling the matrix column by column. Each column represents the output field corresponding to a single input mode, yielding a finite-dimensional approximation to the SM. Extensions of this method allow polarization-resolved measurements, time-resolved acquisition (e.g., via spectral sweeping or ultrafast gating), or reflection matrix capture using a folded interferometric path.

It is notable that while interferometric detection provides full complex-valued measurements, it imposes considerable hardware complexity and sensitivity to drift. As a result, alternative techniques have emerged that reconstruct the SM using intensity-only measurements, often via phase retrieval algorithms or intensity correlation methods [10]. These approaches eliminate the need for a stable reference arm and are more robust to experimental noise, but shift the burden to computational post-processing, often at the expense of speed or accuracy, especially when real-time or dynamic measurements are required [10].

Any experimentally acquired scattering matrix is thus a basis-dependent realization of the underlying operator. Its apparent structure, e.g., sparsity or rank, is contingent on the specific choice of input and output coordinates. For example, the finite numerical aperture (NA) of the detection optics imposes a spatial bandlimit, excluding high-angle components and effectively projecting the output field onto a restricted mode set. As a result, the measured matrix may appear non-unitary even in lossless media, simply because energy has exited the detectable channel space. Furthermore, practical systems rarely have matched input and output dimensionalities: the number of controlled illumination modes (SLM pixels or patterns) and measured output modes (camera pixels) often differ, yielding a rectangular matrix. This dimensional asymmetry precludes direct spectral analysis and requires care when interpreting spectral properties or comparing with theoretical results from mesoscopic transport or random matrix theory, which typically assume square, unitary operators. Measurement noise, amplitude-phase mismatch in SLM encoding, and aberrations in the optical system can further perturb the matrix, often necessitating regularization techniques during inversion or eigenchannel analysis.

2.3 Multimode Fibers

Of particular relevance to the work presented in this thesis are multimode optical fibers (MMFs), whose thin, flexible form factor and ability to support a large number of spatial modes make them attractive for a variety of applications in biomedical imaging, high-capacity optical communications, and quantum information processing [16]. This section provides an overview of the physical principles governing their operation.

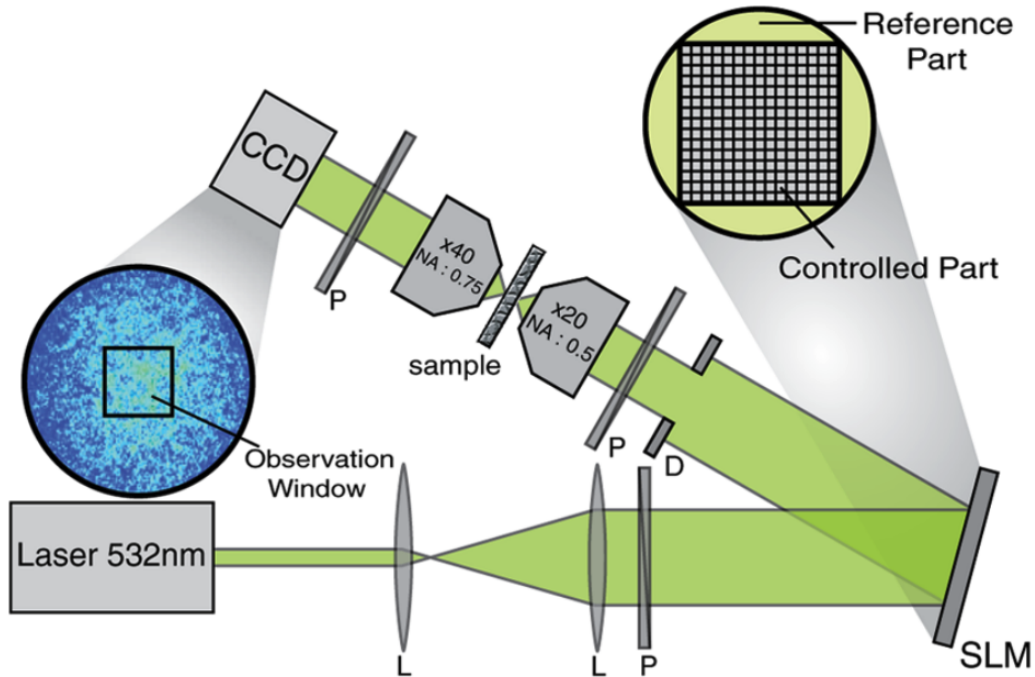


Figure 2.3: Approach used by S. M. Popoff et al. in [12] to measure the transmission matrix of a disordered slab. A laser operating at 532 nm was used to illuminate a sequence of Hadamard patterns generated using a spatial light modulator onto the sample. The output was imaged onto the CCD array. Complex fields were retrieved using phase-shifting interferometry. Figure taken from [12].

2.3.1 Optical Fibers

Optical fibers are dielectric waveguides, typically made of glass or plastic, that confine and transmit light along their length with minimal loss. Their use is widespread across fields including telecommunications, sensing, medical diagnostics, and laser delivery systems [16, 43]. A standard optical fiber consists of a cylindrical core surrounded by a cladding, where the core has a higher refractive index than the cladding. This refractive index contrast enables total internal reflection, the mechanism by which light is confined to the core during propagation.

Depending on the fiber geometry and the wavelength of the incident light, the fiber may support different numbers of guided spatial modes. If the fiber supports only a single transverse mode at a given wavelength, it is referred to as a single-mode fiber (SMF). In contrast, MMFs support a discrete set of orthogonal spatial modes—each representing a unique solution to the wave equation with distinct propagation constants up to multiplicity. These modes can be understood physically as stable transverse field patterns that propagate along the fiber while maintaining their shape, and mathematically as eigenmodes of the Helmholtz equation under the appropriate boundary conditions. Modal dispersion refers to the phenomenon by which even in an ideal MMF, the coherent interference of modes propagating at different phase velocities results in seemingly random speckle patterns [16,

43].

A key parameter governing mode propagation in optical fibers is the normalized frequency, or V-number, which depends on the core radius, the operating wavelength, and the numerical aperture of the fiber as:

$$V = \frac{2\pi a}{\lambda} \text{NA}, \quad (2.55)$$

where a is the fiber's core radius, NA is its numerical aperture, and λ is the operating wavelength. This dimensionless quantity determines how many modes the fiber can support. For step-index fibers, each LP mode has a well-defined cutoff value of the V-number, below which the mode becomes evanescent and ceases to propagate. In the weak-guidance regime, the total number of supported modes is approximately $\frac{V^2}{2}$ including polarization multiplicity.

While SMFs offer stability and simplicity, MMFs offer vastly higher spatial information capacity due to their ability to simultaneously support many spatial channels [16]. However, this increased capacity comes at the cost of greater modal dispersion and intermodal interference, which must be carefully managed, particularly in coherent imaging and transmission systems [16]. In this thesis, a primary focus is on characterizing and exploiting the complex modal structure of MMFs using the framework of scattering theory. Their rich linear operator behavior, stemming from the interference between guided modes and their sensitivity to boundary conditions and perturbations, provides a fertile ground for studying inverse problems and information flow in structured media [16]. Historically, optical telecommunications has favored single-mode fibers due to their lack of spatial modal dispersion and ease of signal integrity management, with multimode fibers largely confined to short-reach or high-power applications where their larger core diameters help mitigate nonlinear effects; however, recent advances in TM-based control and integrated nanophotonic components have opened new possibilities for harnessing the high-dimensional modal capacity of multimode fibers for spatial multiplexing in long-haul and coherent communication systems [16].

2.3.2 Guided Modes of Multimode Fiber

To analyze light propagation in MMFs, the solutions of Maxwell's equations subject to the fiber's cylindrical geometry and refractive index distribution must be considered. These guided modes form a discrete, orthonormal basis of transverse field distributions, each associated with a well-defined longitudinal propagation constant. Their structure is central both to modeling transmission through the fiber and to the operator formalisms underlying wavefront shaping. Following the treatment of Yariv [43], the derivation proceeds by solving the Helmholtz equation in homogeneous media and enforcing boundary conditions determined by the refractive index profile of the fiber. For step-index fibers with piecewise-constant index, the transverse fields satisfy the homogeneous Helmholtz equation in each region (in contrast, for graded-index fibers with continuously varying $n(r)$, the corresponding eigenvalue problem must be solved with the appropriate radial potential).

Due to the fiber's cylindrical symmetry, it is natural to assume a cylindrical coordinate frame (r, ϕ, z) where the transverse dependence separates into radial and angular components [43]. The electromagnetic field components are then \mathbf{E}_r , \mathbf{E}_ϕ , \mathbf{E}_z , \mathbf{H}_r , \mathbf{H}_ϕ and \mathbf{H}_z . Along the

z -axis, the scalar, paraxial Helmholtz equation is

$$(\nabla^2 + k^2) \begin{bmatrix} \mathbf{E}_z \\ \mathbf{H}_z \end{bmatrix} = 0, \quad (2.56)$$

where $k = \frac{\omega^2 n^2}{c^2}$ is the wavenumber, ω , the optical frequency, and c , the speed of light. The Laplacian in cylindrical coordinates is

$$\nabla^2 \equiv \frac{\partial^2}{\partial r^2} + \frac{1}{r} \frac{\partial^2}{\partial \phi^2} + \frac{\partial^2}{\partial z^2}. \quad (2.57)$$

Separation of the transverse spatial variable $\mathbf{r} = (r, \phi)$ from the temporal variable t allows a complex exponential ansatz:

$$\begin{bmatrix} \mathbf{E}(\mathbf{r}, t) \\ \mathbf{H}(\mathbf{r}, t) \end{bmatrix} = \begin{bmatrix} \mathbf{E}(r, \phi) \\ \mathbf{H}(r, \phi) \end{bmatrix} \exp(j(\omega t - \beta z)). \quad (2.58)$$

Applying the ansatz to the harmonic Maxwell's equations yields the following relations [43]:

$$j\omega\epsilon\mathbf{E}_r = j\beta\mathbf{H}_\phi + \frac{1}{r} \frac{\partial}{\partial \phi} \mathbf{H}_z \quad (2.59)$$

$$j\omega\epsilon\mathbf{E}_\phi = -j\beta\mathbf{H}_r - \frac{\partial}{\partial r} \mathbf{H}_z \quad (2.60)$$

$$j\omega\mu\mathbf{E}_z = -\frac{1}{r} \frac{\partial}{\partial \phi} \mathbf{H}_r + \frac{1}{r} \frac{\partial}{\partial r} (r\mathbf{H}_\phi), \quad (2.61)$$

and

$$-j\omega\epsilon\mathbf{H}_r = j\beta\mathbf{E}_\phi + \frac{1}{r} \frac{\partial}{\partial \phi} \mathbf{E}_z \quad (2.62)$$

$$-j\omega\epsilon\mathbf{H}_\phi = -j\beta\mathbf{E}_r - \frac{\partial}{\partial r} \mathbf{E}_z \quad (2.63)$$

$$-j\omega\mu\mathbf{H}_z = -\frac{1}{r} \frac{\partial}{\partial \phi} \mathbf{E}_r + \frac{1}{r} \frac{\partial}{\partial r} (r\mathbf{E}_\phi), \quad (2.64)$$

which allows isolation of $\mathbf{E}_r, \mathbf{E}_\phi$ and corresponding $\mathbf{H}_r, \mathbf{H}_\phi$ in terms of \mathbf{E}_z and \mathbf{H}_z :

$$\mathbf{E}_r = -\frac{-j\beta}{\omega^2\mu\epsilon - \beta^2} \left(\frac{\partial}{\partial r} \mathbf{E}_z + \frac{\omega\mu}{\beta} \frac{\partial}{r\partial\phi} \mathbf{H}_z \right) \quad (2.65)$$

$$\mathbf{E}_\phi = -\frac{-j\beta}{\omega^2\mu\epsilon - \beta^2} \left(\frac{\partial}{r\partial\phi} \mathbf{E}_z - \frac{\omega\mu}{\beta} \frac{\partial}{\partial r} \mathbf{H}_z \right) \quad (2.66)$$

$$\mathbf{H}_r = -\frac{-j\beta}{\omega^2\mu\epsilon - \beta^2} \left(\frac{\partial}{\partial r} \mathbf{H}_z - \frac{\omega\mu}{\beta} \frac{\partial}{r\partial\phi} \mathbf{E}_z \right) \quad (2.67)$$

$$\mathbf{H}_\phi = -\frac{-j\beta}{\omega^2\mu\epsilon - \beta^2} \left(\frac{\partial}{r\partial\phi} \mathbf{H}_z + \frac{\omega\mu}{\beta} \frac{\partial}{\partial r} \mathbf{E}_z \right). \quad (2.68)$$

Assuming ansatzes of the form

$$\mathbf{E}(r, \phi, z) = \psi(r) e^{\pm il\phi} e^{i\beta z} \quad (2.69)$$

$$\mathbf{H}(r, \phi, z) = \chi(r) e^{\pm il\phi} e^{i\beta z}, \quad (2.70)$$

the radial equation for $\psi(r)$ becomes

$$\frac{d^2\psi}{dr^2} + \frac{1}{r} \frac{d\psi}{dr} + \left(k^2 - \beta^2 - \frac{l^2}{r^2} \right) \psi = 0. \quad (2.71)$$

Define

$$h^2 \equiv k^2 - \beta^2, \quad (2.72)$$

$$q^2 \equiv \beta^2 - k^2. \quad (2.73)$$

Then, for $k^2 > \beta^2$ ($h^2 > 0$),

$$\psi(r) = A J_l(hr) + B Y_l(hr), \quad (2.74)$$

where J_l and Y_l are Bessel functions of the first and second kind, respectively, of order l . For $k^2 < \beta^2$ ($q^2 > 0$) the solutions are

$$\psi(r) = C I_l(qr) + D K_l(qr), \quad (2.75)$$

where I_l and K_l are modified Bessel functions of the first and second kind, respectively, of order l . By enforcing the continuity of the tangential field components at the core-cladding interface, only discrete values of the propagation constant β satisfy the boundary conditions. These eigenvalue solutions define the guided modes $\{\psi_m(r, \phi)\}$, which, with suitable normalization, form an basis for representing any field propagating inside the fiber.

In these mode solutions, exponential term $\exp(il\phi)$ encodes the azimuthal phase structure of the mode, corresponding to an orbital angular momentum index l , while $\psi(r)$ determines how the mode's energy is distributed radially across the fiber cross-section. Different combinations of $\psi(r)$ and l define distinct guided modes, each with their own propagation constants, field symmetries, and confinement characteristics. In this framework, modes are often classified as lower- or higher-order depending on their azimuthal and radial indices. Lower-order modes have field distributions concentrated near the fiber core center and thus generally exhibit the highest confinement. Higher-order modes, with larger l or p indices, have more complex transverse structures with multiple intensity lobes, extend further into the cladding, and are more sensitive to bending and fiber imperfections. These differences play a critical role in modal coupling and dispersion in practical fibers, where higher-order modes are often harder to excite and more prone to loss. The spatial field profiles of the modes are determined by the fiber's refractive index distribution, which sets the boundary conditions for the Helmholtz equation. For example, in step-index fibers, the refractive index changes abruptly at the core-cladding boundary, resulting in modes with distinct propagation constants and more pronounced differences in group velocity. This leads to stronger modal dispersion and less overlap between modes. Conversely, graded-index (GRIN) fibers feature a gradual, typically parabolic, refractive index decrease from the core center outward, which causes modes to experience more similar effective refractive indices. This index grading equalizes modal group velocities, reducing dispersion and enabling modes to maintain more stable phase relationships over longer distances. These differences in index profile fundamentally shape the spatial and temporal behavior of mode families, influencing the fiber's transmission characteristics.

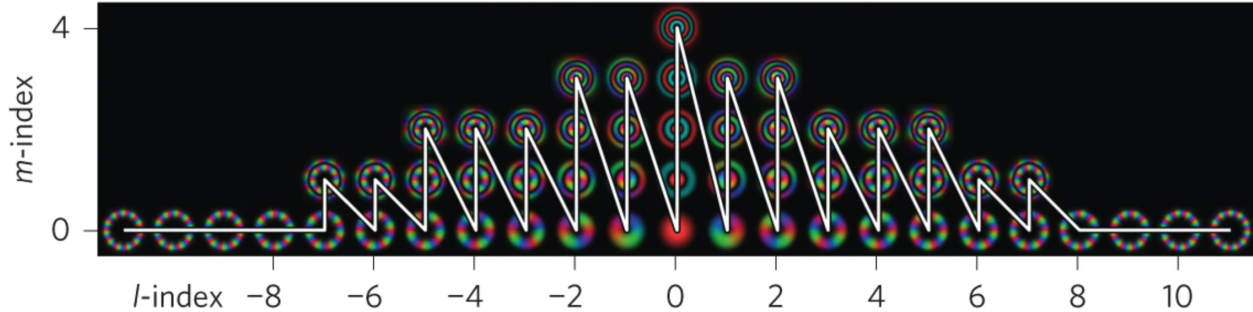


Figure 2.4: Mode pyramid showing the spatial electromagnetic profiles of the eigenmodes of a step-index multimode fiber. The horizontal m -axis corresponds to the radial mode index, defining the confinement and radial distribution. The vertical l -index defines the azimuthal phase structure and thus the orbital angular momentum of the mode as $\frac{l\hbar}{2}$ per photon. Figure taken from [17].

Moreover, depending on the fiber’s symmetry and the application, guided modes may be represented in different complete sets such as Laguerre–Gaussian (LG) or Hermite–Gaussian (HG) modes [9]. These sets are related through basis transformations but highlight different physical features; LG modes make the orbital angular momentum content explicit, while HG modes are suited to rectangular or asymmetric structures. In optical fibers with weak refractive index contrast—often called the weakly guiding regime—the longitudinal components of the electric and magnetic fields become negligible compared to the transverse components. This simplifies Maxwell’s equations to a scalar wave equation, whose solutions can be expressed as orthogonally polarized field patterns known as linearly polarized (LP) modes. LP modes are labeled by two integers: l , the azimuthal index describing the number of field variations around the circumference, and p , the radial index counting the number of intensity maxima in the radial direction. They are closely related to their full-vector counterparts but ignore small polarization–spatial coupling effects, making them a convenient and widely used basis for modeling and experimental work in multimode fibers.

In practice, modes are often arranged in a “mode pyramid,” where groups of modes with the same radial and azimuthal indices share similar propagation constants and are often nearly degenerate. An example of a mode-pyramid corresponding to the LP modes of a step-index MMF is shown in Fig. 2.4, borrowed from [17]. This visualization helps illustrate the hierarchy of mode families, such as LG, LP, HG modes, and clarifies how increasing either the azimuthal or radial indices changes the mode’s spatial complexity. Proximity in the mode pyramid also indicates closely matched phase velocities, making such modes more susceptible to coupling through perturbations such as bending or core imperfections.

2.3.3 Transmission Matrix of Multimode Fiber

The complexity of modal behavior in MMF means that light transport cannot be realistically captured by tracking individual modes in isolation; propagation is the result of coherent interference among many modes, with modal crosstalk induced by bends, refractive index fluctuations, thermal and mechanical vibrations, and so on. The TM thus offers a natural linear operator framework to capture all of these effects in aggregate, mapping any input

field to its output without requiring explicit knowledge of the intermediate modal dynamics for a given fiber.

The mode basis provides a physically meaningful and analytically convenient coordinate system for representing wave propagation in MMF. In this basis, the MMF maps the complex amplitudes of guided modes at the input facet to those at the output facet. In an ideal fiber—free of coupling, disorder, or perturbation—this operator is diagonal, with each mode accumulating only a deterministic phase delay during propagation. In an ideal fiber with neither coupling nor disorder, the operator is diagonal, with each mode acquiring only a phase delay. In practice, however, bending and residual index fluctuations introduce off-diagonal terms that redistribute power among modes. The strength and axial scale of this redistribution depend on the perturbation spectrum and on the spatial overlap of the interacting modal fields; a convenient figure of merit is the mode-coupling length—the distance over which appreciable power exchange occurs. In typical step-index MMF subjected to modest bending or stress, coupling lengths of millimeters to a few centimeters are observed, so that mode mixing becomes a dominant effect over technologically relevant distances [17, 18]. Moreover, higher-order modes often experience higher loss due to their greater spatial extent, especially near the cladding boundary. These effects not only attenuate the signal but can also distort the modal distribution, further complicating attempts to reconstruct or transmit structured light fields through the fiber. Apart from mode effects, polarization coupling is also significant in real-world MMF, to the extent to which spatial and polarization profiles can be totally controlled by one another using wavefront shaping approaches [44].

The TM also allows physical insight into the mechanisms by which different effects, such as bending, change propagation in the MMF, by characterizing them as operators acting on the TM itself. Rigorous experimental investigation of bending in MMF, using the TM was first conducted by Plöschner et al. (2015) [17]. Their findings suggest that the dominant effect induced by a small amount of bending is a mode-dependent phase delay [17]. That is, the LP mode-basis TM remained diagonal but was left-multiplied by a phase-only diagonal matrix; this is in agreement with the theoretical prediction for LP modes in step-index fiber. For more significant bending, the mode profiles themselves changed according to a perturbative model. The total TM is modeled as a product of bent segments.

2.4 Matrix Analysis and Operator Theory

A central focus of this thesis is the operator-theoretic perspective of scattering in complex media. Rather than treating TMs or RMs as a finite matrix of empirical coefficients, their origin as an infinite-dimensional mathematical operators is considered. This perspective allows analysis of symmetries, spectral properties, and physical constraints from first principles. As such, some mathematical background is covered here, the knowledge of which is useful in interpreting subsequent sections. The reader is referred to [36] and [45] for more thorough and rigorous expositions.

2.4.1 Basic Definitions

Underlying linear algebra and functional analysis are vector spaces defined over a field F . A vector space V is a collection of elements, called vectors, that is closed under a binary operation called addition, which is associative, commutative, and has both an identity element and additive inverses. V must also support scalar multiplication by elements of F , which is distributive, associative, and compatible with the field identities. The set of n -tuples over F , denoted F^n , forms a vector space under element-wise addition and scalar multiplication. Of particular importance are the real and complex n -tuples, denoted \mathbb{R}^n and \mathbb{C}^n respectively, which serve as standard finite-dimensional vector spaces.

A basis \mathcal{B} of V is a collection of elements that span V ; that is to say, that every element in V can be written as a unique linear combination of elements in \mathcal{B} . For example, the 3-tuples $S = \{[1, 0, 0]^T, [0, 1, 0]^T, [0, 0, 1]^T\}$ form a basis for \mathbb{R}^3 (\mathbb{C}^3) because any 3-tuple can be written as a sum of the vectors in S scaled by real (complex) coefficients [36]. A basis must have the property that if any single element is removed, some elements in V cannot be represented as linear combinations of the resulting set. Every vector space has a basis. In most vector spaces, there are many possible bases [36].

A linear operator $T : U \rightarrow V$ is a mapping between vector spaces U and V such that

$$\forall x_1, x_2 \in U, a_1, a_2 \in F, T(a_1x_1 + a_2x_2) = a_1T(x_1) + a_2T(x_2) \in V. \quad (2.76)$$

Linear operators are represented by matrices, which are rectangular arrays of elements of F . A matrix $\mathbf{A} \in \mathbf{M}^{m \times n}(F)$ represents T relative to some set of bases \mathcal{B}_1 and \mathcal{B}_2 that span U and V . Addition is defined only between matrices of the same size, and corresponds to element-wise addition on the scalar elements of each matrix as dictated by F . The additive identity is the so-called zero matrix, which has all elements equal to the additive identity of F (e.g., 0). Matrix multiplication corresponds to the composition of linear transformations. Multiplication between matrices $\mathbf{A} \in \mathbf{M}^{m \times n}(F)$ and $\mathbf{B} \in \mathbf{M}^{n \times q}(F)$, denoted \mathbf{AB} , is defined only when $n = p$, and is associative but not, in general, commutative. The multiplicative identity of dimension n is denoted \mathbf{I}_n . The product \mathbf{AB} is constructed by multiplying rows of A with the columns of B .

An inner product on a vector space V over a field F (typically \mathbb{R} or \mathbb{C}) is a function $\langle \cdot | \cdot \rangle : V \times V \rightarrow F$ that assigns a scalar to each pair of vectors. When defined over \mathbb{R}^n or \mathbb{C}^n , the standard inner product takes the form $\langle \mathbf{v} | \mathbf{w} \rangle = \mathbf{v}^\dagger \mathbf{w}$, where $\mathbf{v}, \mathbf{w} \in V$. Inner products endow vector spaces with geometric structure, allowing the definition of length, angle, and orthogonality. Two vectors \mathbf{v} and \mathbf{w} are said to be orthogonal if their inner product is the additive identity of F (e.g., 0). Vector spaces endowed with an inner product are called Hilbert spaces, and form the natural analytic setting in many areas of science and engineering.

2.4.2 Eigenvalue and Singular Value Decompositions

For a matrix $\mathbf{A} \in \mathbb{C}^{n \times n}$, the following equation is considered:

$$\mathbf{Ax} = \lambda \mathbf{x}; \quad \mathbf{x} \neq 0, \quad (2.77)$$

where $\lambda \in \mathbb{C}$. If a vector $\mathbf{x} \in \mathbb{C}^n$ satisfies this, it is called an eigenvector of \mathbf{A} , and λ is its associated eigenvalue. Conceptually, an eigenvector corresponds to a principal direction of

the linear transformation represented by \mathbf{A} ; that is, one in which the transformation merely scales. A matrix may not have any eigenvectors. The set of all eigenvalues is called the spectrum of \mathbf{A} . If \mathbf{A} has n linearly independent eigenvectors, it is similar to a diagonal matrix. The diagonalization of \mathbf{A} is called its eigenvalue decomposition, and is then written as

$$\mathbf{A} = \mathbf{P} \cdot \mathbf{\Lambda} \cdot \mathbf{P}^{-1} \quad (2.78)$$

+ The columns of the matrix \mathbf{P} contain the eigenvectors of \mathbf{A} , and $\mathbf{\Lambda}$ is a diagonal matrix whose entries are the corresponding eigenvalues. Diagonalization conceptually corresponds to shifting a matrix to the appropriate principal basis, in which its action is simply scaling, and then shifting back to the original basis. Many operations on \mathbf{A} (e.g. computing powers of \mathbf{A}) can be drastically simplified to operations on $\mathbf{\Lambda}$. This makes diagonalization highly useful in practice.

In specific cases, all the eigenvectors of A may be orthogonal to each other. Then, \mathbf{P} is unitary, i.e., $\mathbf{P} \cdot \mathbf{P}^\dagger = \mathbf{P}^\dagger \cdot \mathbf{P} = \mathbf{I}_n$. $\mathbf{\Lambda}$ is then called a normal matrix.

The singular value decomposition (SVD) of a matrix $\mathbf{A} \in \mathbb{C}^{m \times n}$ is:

$$\mathbf{A} = \mathbf{U} \cdot \mathbf{\Sigma} \cdot \mathbf{V}^\dagger, \quad (2.79)$$

where \mathbf{U} and \mathbf{V} are unitary and $\mathbf{\Sigma}$ is nonnegative, real, and diagonal. The columns of \mathbf{U} contain the so-called left singular vectors, those of \mathbf{V} contain the right singular vectors, and the diagonal elements of $\mathbf{\Sigma}$ are called singular values.

The SVD and eigenvalue decomposition are similar in concept but have several key differences. The singular value decomposition exists for any matrix of any size, whereas the eigenvalue decomposition exists only for full-rank, square matrices. In general, the singular values and eigenvalues of a matrix may not be related; however, for normal matrices, the former are the absolute values of the latter. In physical terms—particularly in optical scattering or imaging—the singular values often correspond to physically measurable quantities such as energy throughput or gain, while the eigenvalues reflect internal phase and modal behavior.

Chapter 3

Reciprocity-based Compensation of Aberrations

3.1 Aberrations in Optical Systems

3.1.1 Origin of Aberrations

In classical optical theory, rays emanating from an object are brought to a single image point [43]. This behavior is described under the paraxial approximation, in which rays lie close to the optical axis and form small angles with it. Under these conditions, sines may be replaced by their angular arguments, and the system response becomes linear in both ray height and angle [43]. The resulting formalism, known as geometric optics, predicts a one-to-one mapping between object and image points, governed by the cardinal points of the system. Optical aberrations arise when this approximation breaks down or when imperfections in the optical elements perturb the ideal ray paths. They represent departures from paraxial predictions and may be viewed as higher-order corrections to the first-order model.

A more general wave-optical perspective identifies aberrations with phase distortions imposed on ideal spherical or planar wavefronts [1]. In the ideal case, a coherent optical system transmits a wavefront that converges to a focus with uniform phase. In practice, however, misalignment, surface irregularities, or inhomogeneities in refractive index introduce systematic phase or amplitude errors across the aperture. These distortions broaden, shift, or deform the resulting point spread function. As a result, the images formed may be spatially shifted, enlarged, or blurred, corresponding to the degree and type of aberration [1].

More generally, the term "aberration" is also used to describe any deviation from ideal wavefront propagation, including those caused by complex or disordered media. For instance, in biological tissue, refractive index variations and multiple scattering events distort the incident wavefront as it penetrates the medium. These sample-induced aberrations compromise image resolution and contrast at depth by scrambling the spatial and phase information of the incoming light, making it difficult to distinguish signal from background. Imaging in such environments requires compensation of these aberrations to recover the desired spatial information.

3.1.2 Correction of Aberrations in Experimental Systems

To characterize and correct low-order experimental aberrations, it is common to expand the pupil-plane phase distortion in a suitable orthonormal basis. The most widely used basis in optical systems with circular symmetry is the Zernike polynomials: a complete set of real-valued functions defined on the unit disk, orthogonal under the standard inner product weighted by radial area [1] (Fig. 3.1). Each Zernike mode corresponds to a specific spatial phase profile and admits a direct geometric interpretation. The lowest-order term represents a constant phase offset (piston), followed by linear gradients corresponding to tip and tilt, quadratic curvature representing defocus, and higher-order modes such as astigmatism, coma, and spherical aberration. Conveniently, these low-order Zernike terms model common experimental effects that may cause deviations from the expected behavior of an optical system.

Because of their compact representation and physical interpretability, Zernike modes are widely employed in wavefront sensing, adaptive optics, and aberration correction, particularly in microscopy and biomedical imaging. Aberrations are typically estimated by fitting a few Zernike modes to the measured data, which can then be nulled by a deformable mirror or digital phase-conjugation scheme. They may also be incorporated into computational correction schemes during the measurement of transmission or reflection matrices in systems involving scattering media. In this context, the goal is to isolate sample-induced effects from distortions introduced by the experimental apparatus, enabling accurate characterization of the medium under examination.

3.2 Reciprocity in Scattering Optics

The scattering matrix, \mathbf{S} , of an optical system describes the amplitude and phase relationship between a set of input and output flux-carrying modes. It is represented with sub-blocks corresponding to reflection from the same side (\mathbf{r}, \mathbf{r}') and transmission in opposite directions (\mathbf{t}, \mathbf{t}'):

$$\mathbf{S} = \begin{bmatrix} \mathbf{r} & \mathbf{t}' \\ \mathbf{t} & \mathbf{r}' \end{bmatrix} \quad (3.1)$$

In the absence of active or nonlinear elements, light propagation through a reciprocal medium satisfies a fundamental symmetry: the response observed when source and detector are exchanged remains invariant [10, 31–33]. This reciprocity principle is described by the Lorentz reciprocity theorem, which asserts that the Green’s function of a linear, time-invariant, and source-free medium is symmetric under exchange of spatial arguments. In such regimes, the scattering matrix obeys transpose-symmetry: $\mathbf{S} = \mathbf{S}^T$. This imposes the relations $\mathbf{r} = \mathbf{r}^T$, $\mathbf{r}' = \mathbf{r}'^T$, and $\mathbf{t}' = \mathbf{t}^T$. Moreover, double-pass through a medium, which is a composed forward and backward operation $\mathbf{t}^T \cdot \mathbf{t}$, is symmetric.

In practical measurements, however, these symmetries are often violated. Small but systematic discrepancies arise within forward and reverse transmission matrices, or between reflection measurements that should, in principle, obey the constraints imposed by reciprocity. These deviations are not intrinsic to the medium under study, but instead originate from

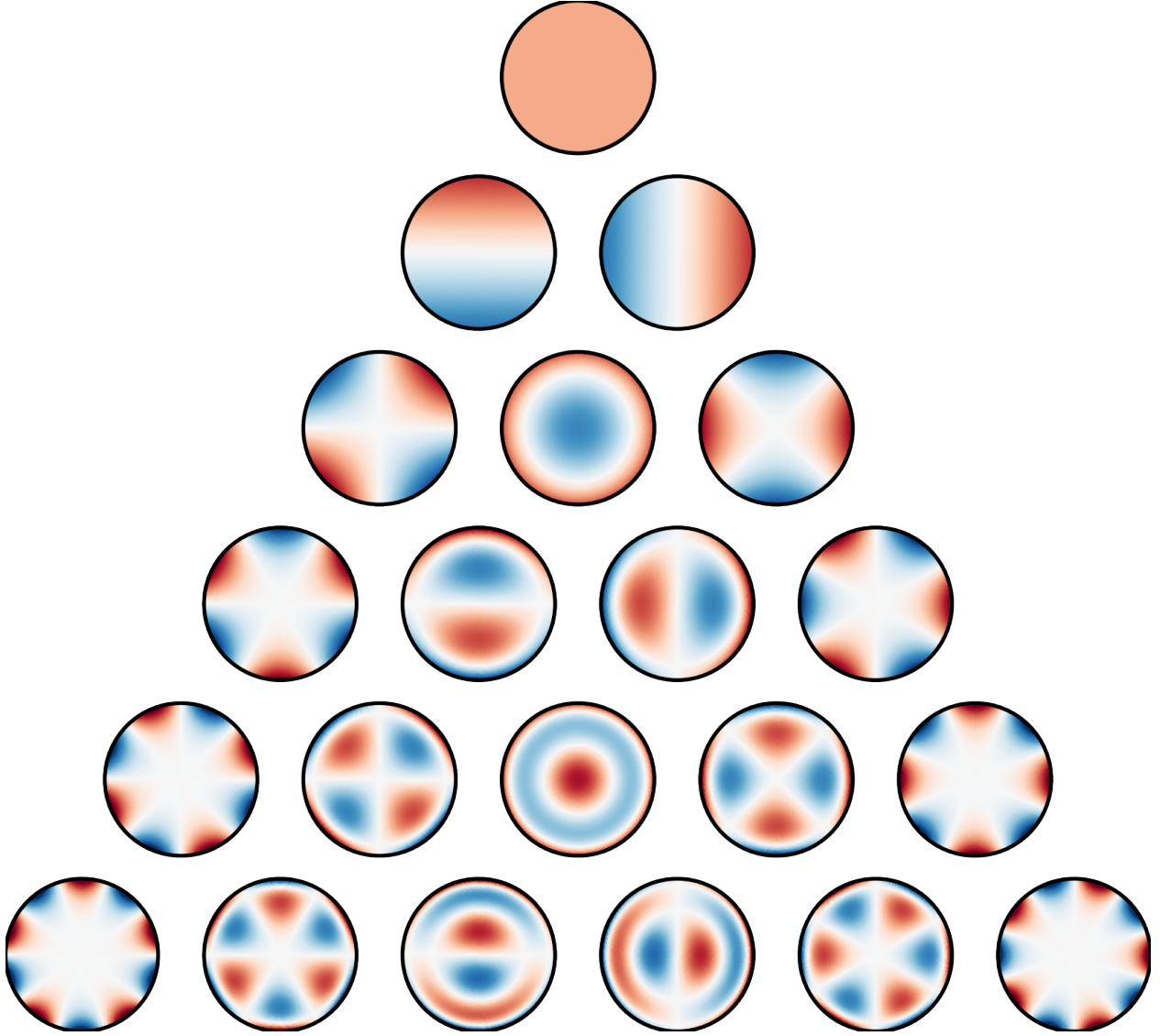


Figure 3.1: Pyramid showing the first 21 Zernike polynomials, a set of orthonormal basis functions defined on the unit disk and commonly used for compensation of optical aberrations. Figure taken from Wikipedia [46].

imperfections in the experimental apparatus. Most measurement setups excite the medium along one optical path and detect along another—for example, using SLM modes for illumination and camera pixels for detection. Consequently, the only segment of the optical path that strictly obeys reciprocity is the portion within the scattering medium itself. Aberrations such as optical misalignment, defocus, astigmatism, and index mismatch at interfaces introduce phase distortions that differ between the two paths, leading to asymmetries in the measured field. Though often stable and low-order, these system-induced aberrations manifest as violations of reciprocity at the matrix level. That is, an experimental reflection measurement $\tilde{\mathbf{r}} \neq \tilde{\mathbf{r}}^T$ unless the system-induced aberrations are properly compensated.

The central observation underlying the present approach is that this asymmetry may

be minimized by applying a suitable correction term to the input or output channels. By iteratively adjusting a wavefront operator so as to restore reciprocity in the measured transmission or reflection matrices, one may estimate and correct the dominant system aberrations. This procedure requires no knowledge of the object or medium under study, and operates solely on the internal symmetries of the linear system imposed by reciprocity. In the following section, this principle is developed into an explicit correction method. The correction is represented as a multiplicative factor across spatial and polarization channels, and is optimized to minimize a loss function corresponding to reciprocity violation.

3.3 Methods and Results

3.3.1 Measurement of Transmission and Reflection Matrices

To evaluate the proposed approach, measurements of transmission (TM) and reflection matrices (RM) of complex media were conducted. The methodology by which this was done is now briefly covered.

The first experimental demonstration of coherent TM measurement through a multiply-scattering slab was reported by Popoff et al. [12], in which a series of phase-modulated input wavefronts, generated using a spatial light modulator, was transmitted through the medium. The resulting output electric field was measured interferometrically, allowing for full field retrieval. In that work, the input basis consisted of Hadamard phase patterns, which provide an orthogonal and energy-efficient set well-suited to SLM-based modulation. In principle, the TM can be measured using any set of input patterns and a coherent output detection scheme, as the objective is simply to characterize the linear input–output relationship relative to a chosen basis. The specific implementation, such as the choice of modulation basis and interferometric method, depends on a range of practical considerations, including equipment availability, properties of the scattering medium, measurement speed, and stability.

An important point is that camera intensity images are not enough to deduce the full amplitude and phase of a complex-valued optical field. Here, off-axis holography was employed to interferometrically gain access to the full amplitude and phase data embedded in the measured matrices [47]. The concept behind the approach is briefly covered for completeness, based on the article written by S. Popoff [48]. The curious reader is directed to that article for a more thorough explanation and helpful simulations. In off-axis holography, the field whose amplitude and phase is unknown is made to interfere with a plane wave at some incident angle. Denoted by \mathbf{E}_0 and \mathbf{E}_s are the reference and sample fields, respectively, which belong to the same polarization state, and by θ their incidence angle. The measured intensity on the camera is:

$$\mathbf{I} = |\mathbf{E}_0|^2 + |\mathbf{E}_s|^2 + \mathbf{E}_0 \bar{\mathbf{E}}_s e^{ikx \sin \theta} + \bar{\mathbf{E}}_0 \mathbf{E}_s e^{-ikx \sin \theta}. \quad (3.2)$$

In the spatial frequency domain, one observes that the first two terms are mere constants that occupy the center lobe. Whereas, the final two terms are centered around the spatial frequencies $\mathbf{k}_+ = \frac{k \sin \theta}{2\pi}$ and $\mathbf{k}_- = \frac{-k \sin \theta}{2\pi}$, respectively. Moreover, the second lobe, centered around \mathbf{k}_- , is directly proportional to \mathbf{E}_s , the sample field phasor. Demodulating this lobe

such that it is centered in the frequency domain, and applying the inverse Fourier transform computationally yields directly the optical field.

The experiments conducted involved the measurement of optical transmission and reflection matrices (TMs and RMs, respectively) of disordered media. In particular, the single-pass forward and double-pass TMs of MMF, denoted \mathbf{T}_{fw} and $\mathbf{T}_{2\times}$, respectively, were measured. In single-pass, the input-output relationship corresponding to light that has traveled once through the fiber is measured. In double-pass, light that Fresnel-reflects off the distal end and travels back through the fiber is measured. Furthermore, the RM of a multiply-scattering slab was measured, denoted \mathbf{R} , corresponding to a same-side input-output relationship between incident and reflected fields. Reciprocity imposes that $\mathbf{T}_{2\times}$ and \mathbf{R} are transpose-symmetric. $\mathbf{T}_{2\times}$ consists of successive transmission through the forward path \mathbf{T}_{fw} and its reverse, \mathbf{T}_{fw}^T , so reciprocity additionally imposes that $\mathbf{T}_{2\times} = \mathbf{T}_{\text{fw}}^T \cdot \mathbf{T}_{\text{fw}}$.

In the present investigation, the following scheme for TM and RM measurement was applied (shown in Fig. 3.2). A wavelength-tunable semiconductor laser (L, TSL-570, Santec) with < 100 KHz linewidth and tuning range from 1260 nm to 1360 nm was used as the source. Apart from multi-spectral measurements explicitly described in later sections, the operating wavelength of the laser was 1310 nm. The fiber-coupled laser output was split into sample and reference arms in a Mach-Zehnder interferometer configuration. In the sample arm, a two-dimensional galvanometric mirror scanner (GMs, GVSM002, Thorlabs) was used to sequentially scan a focal spot across a lateral grid to define a 16×16 grid of input spatial channels. For each spatial position, the polarization state was switched between horizontal (H) and vertical (V) linear states using a fiber-coupled electro-optic phase retarder (PR, PRT1010, Boston Applied Technologies Inc.). The proximal facet of the MMF, or scattering slab, was kept at the focal plane of the first objective lens (OL1, NIR Infinity Corrected, Mitutoyo). For single-pass MMF TM measurements, the distal facet was placed at the focal plane of a second objective lens (OL2, NIR Infinity Corrected, Mitutoyo). The distal facet of the fiber was imaged onto the camera after interfering with the reference wave and being split into orthogonal polarization components using a beam displacer (BD, BD40, Thorlabs). For double-pass MMF TM or RM measurements, the flip mirror was toggled such that light was redirected to be imaged onto the camera by OL1 and a beam-splitter (BS1). Detection was performed with an InGaAs camera (OW1.7-VS-CL-LP-640, Raptor Photonics), with 20 μs exposure time and a maximum frame rate of 120 Hz. Off-axis digital holography was employed to recover the complex field. A fixed reference input mode was revisited after each input mode during TM acquisition to enable phase tracking and compensate for phase drift. Recorded interference patterns were demodulated by correcting for the spectral variation of the off-axis carrier and aligned using the phase-tracking data. The output fields were flattened into column vectors and assembled into a full TM or RM, represented as a block-Jones matrix \mathbf{M} :

$$\mathbf{M} = \begin{bmatrix} \mathbf{M}_{HH} & \mathbf{M}_{HV} \\ \mathbf{M}_{VH} & \mathbf{M}_{VV} \end{bmatrix} \quad (3.3)$$

where the sub-block indices correspond to detection and illumination polarization state, in that order. MMF measurements were done using a 0.22 ± 0.02 NA, 50 μm diameter, step-index MMF (FG050LGA, Thorlabs), and a plastic eraser (Hi Polymer, Pentel) was used as a scattering slab.

Due to optical aberrations, the measured TMs and RMs of complex media often violate the symmetry constraints imposed by reciprocity. This discrepancy can be exploited as a diagnostic: since reciprocity must hold for any linear, source-free system, the violation of transpose symmetry in measured TMs or RMs points to distortions external to the medium. Reciprocity thus provides a physical constraint for correcting aberrations introduced by the optical elements in asymmetric illumination and detection paths. A similar exploration of reciprocity-induced symmetries in MMF TMs was previously undertaken in our group [49]. In that work, single- and double-pass TMs were measured for a single polarization state, and aberrations were corrected via a low-order Zernike decomposition. The symmetry of the round-trip matrix was used to assess reciprocity, and the agreement between the forward and double-pass measurements served as a metric for calibration quality. The present study builds upon this idea but proceeds along a distinct line. Rather than imposing a Zernike basis a priori, reciprocity itself is employed as a self-consistency condition, using it to directly optimize the input wavefront. In doing so, the dominant aberration modes — including tilt — emerge naturally from the procedure. This allows for aberration correction without explicit modal decomposition and extension to the full vectorial case demonstrated here. Moreover, the procedure is not limited to guided media. Measurements were performed both in MMFs as well as in a multiply scattering slab, demonstrating the generality of the reciprocity constraint. The resulting agreement between single- and double-pass TMs offers further confirmation of the correction procedure. The present formulation offers a distinct route to reciprocity enforcement, applicable across systems and polarizations, and requires no assumptions on the aberration structure.

3.3.2 Correction of Symmetric Operators

Correction Ansatz and Optimization Problem Formulation

The analysis begins with symmetric operators, such as the double-pass TM of a multimode fiber or the RM of a scattering slab, where reciprocity implies matrix transpose-symmetry. A correction operator \mathbf{X}_R is introduced, and the corresponding optimization problem is formulated by penalizing deviations from this constraint:

$$\min \|\mathbf{R} - \mathbf{R}^T\|_F^2, \quad (3.4)$$

where the corrected matrix $\mathbf{R} = \mathbf{X}_R \cdot \tilde{\mathbf{R}}$ is formed by left multiplication of the experimentally measured matrix, $\tilde{\mathbf{R}}$, by \mathbf{X}_R , and $\|\cdot\|_F$ denotes the Frobenius norm. \mathbf{X}_R was then iteratively optimized using matrix gradient descent, as explained in detail below.

While the initial gradient updates of \mathbf{X}_R exhibited a predominantly diagonal structure in each polarization sub-block of the scattering operators—consistent with physically plausible, spatially local phase aberrations—subsequent iterations introduced off-diagonal elements that grew in magnitude and lacked spatial structure. To better constrain the solution space, the system’s behavior was incorporated: polarization rotation effects were assumed to originate primarily in the near field, due to fiber coupling and upstream optical elements in the illumination path, and the detection-path imaging system—comprising primarily free-space propagation and isotropic refractive elements—were presumed to be polarization-preserving to leading order. This structure, combined with the imaging geometry of the system, suggested

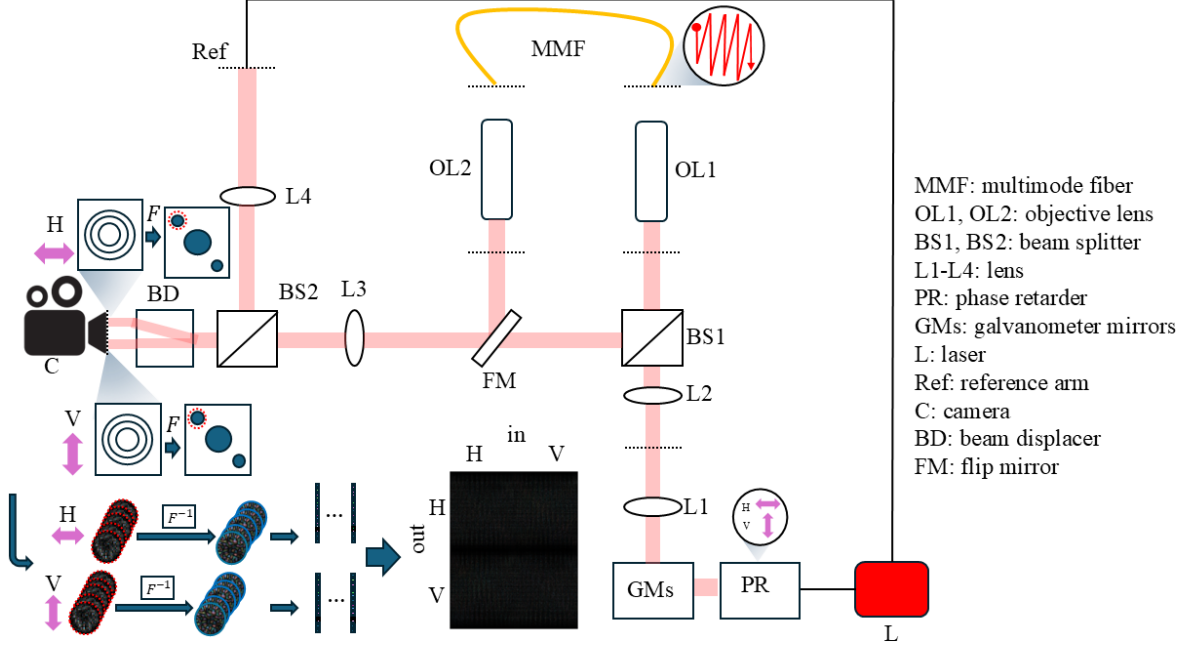


Figure 3.2: Experimental setup and procedure used in the present investigation to measure transmission and reflection matrices of complex optical media. The sample under examination was scanned with a grid of focal spots, and the output complex field was measured using off-axis holography.

a decomposition of the aberrations into near- and far-field components, denoted Ψ and Φ respectively. Ψ captured near-field polarization effects with diagonal structure within each polarization-conversion block, indicating locally varying phase delays without spatial mode-mixing. Φ modeled far-field aberrations, enforced via diagonal Φ_H and Φ_V components and vanishing off-diagonal coupling:

$$\Psi = \begin{bmatrix} \Psi_{HH} & \Psi_{HV} \\ \Psi_{VH} & \Psi_{VV} \end{bmatrix} \quad (3.5)$$

$$\Phi = \begin{bmatrix} \Phi_H & \mathbf{0} \\ \mathbf{0} & \Phi_V \end{bmatrix}, \quad (3.6)$$

and the full correction operator ansatz was built as:

$$\mathbf{X}_R = \mathbf{F}^\dagger \cdot \Phi \cdot \mathbf{F} \cdot \Psi, \quad (3.7)$$

where \mathbf{F} and \mathbf{F}^\dagger denote the forward and inverse transformations between the spatial and spatial frequency domains, respectively. Since the underlying scattering operators are dyadic tensors [2], \mathbf{F} and \mathbf{F}^\dagger are not the canonical discrete Fourier transform matrices but are instead built by vectorizing the appropriate two-dimensional field relationships.

Complex-valued Matrix Wirtinger Gradients

Matrix gradient descent was applied to find optimal values of Φ and Ψ . To compute gradients efficiently, Wirtinger calculus was used to derive analytical expressions for the complex derivatives. This avoids the computational burden of numerical differentiation, which becomes prohibitive and numerically unstable for large-scale matrices. Wirtinger derivatives extend the notion of differentiation to functions of complex variables, providing a framework for constructing gradients that remain valid even when an objective function is not holomorphic [50–52]. This approach yields analytically tractable gradients compatible with standard optimization algorithms, enabling solutions to inverse problems involving functions of several complex variables. For a real-valued function $f : \mathbb{C}^{n \times n} \rightarrow \mathbb{R}$ of a complex matrix $\mathbf{A} \in \mathbb{C}^{n \times n}$, the Wirtinger gradient is given by [52]

$$\nabla f = \frac{\partial f}{\partial \Re[\mathbf{A}]} + j \frac{\partial f}{\partial \Im[\mathbf{A}]} \quad (3.8)$$

$$= 2 \frac{\partial f}{\partial \mathbf{A}}, \quad (3.9)$$

where \Re and \Im denote the real and imaginary parts of \mathbf{A} , respectively. The following analysis derives the matrix Wirtinger gradients for each variable component of the assumed ansatz, \mathbf{X}_R , i.e., Ψ and Φ , for use in the gradient descent routine.

Using the fact that the Frobenius norm of a matrix \mathbf{A} can be expressed using the matrix trace tr as $\text{tr}(\mathbf{A}^\dagger \cdot \mathbf{A})$, the loss function $\|\mathbf{R} - \mathbf{R}^T\|_F^2$ can be expressed as

$$f = \text{tr} \left[\left((\mathbf{F}^\dagger \cdot \Phi \cdot \mathbf{F} \cdot \Psi) \cdot \tilde{\mathbf{R}} - \tilde{\mathbf{R}}^T \cdot (\mathbf{F}^\dagger \cdot \Phi \cdot \mathbf{F} \cdot \Psi)^T \right)^\dagger \cdot \left((\mathbf{F}^\dagger \cdot \Phi \cdot \mathbf{F} \cdot \Psi) \cdot \tilde{\mathbf{R}} - \tilde{\mathbf{R}}^T \cdot (\mathbf{F}^\dagger \cdot \Phi \cdot \mathbf{F} \cdot \Psi)^T \right) \right] \quad (3.10)$$

Since stationary points of the loss function occur when $\frac{\partial f}{\partial \Psi} = 0$ and $\frac{\partial f}{\partial \Phi} = 0$, the second term, $\mathbf{R} - \mathbf{R}^T$, does not contribute to the gradient. Hence, f may be expressed as

$$f = \text{tr} \left[\left(\tilde{\mathbf{R}}^\dagger \cdot \bar{\Psi} \cdot \mathbf{F}^\dagger \cdot \bar{\Phi} \cdot \mathbf{F} \right) \cdot \mathbf{K} - \mathbf{F}^T \cdot \bar{\Phi} \cdot \bar{\mathbf{F}} \cdot \bar{\Psi} \cdot \tilde{\mathbf{R}} \right) \cdot \mathbf{K} \right] \quad (3.11)$$

$$\equiv \text{tr} \left[\mathbf{F} \cdot \mathbf{K} \cdot \tilde{\mathbf{R}}^\dagger \cdot \bar{\Psi} \cdot \mathbf{F}^\dagger \cdot \bar{\Phi} \right] - \text{tr} \left[\bar{\mathbf{F}} \cdot \bar{\Psi} \cdot \tilde{\mathbf{R}} \cdot \mathbf{K} \cdot \mathbf{F}^T \cdot \bar{\Phi} \right] \quad (3.12)$$

$$\equiv \text{tr} \left[\mathbf{F}^\dagger \cdot \bar{\Phi} \cdot \mathbf{F} \cdot \mathbf{K} \cdot \tilde{\mathbf{R}}^\dagger \cdot \bar{\Psi} \right] - \text{tr} \left[\tilde{\mathbf{R}} \cdot \mathbf{K} \cdot \mathbf{F}^T \cdot \bar{\Phi} \cdot \bar{\mathbf{F}} \cdot \bar{\Psi} \right], \quad (3.13)$$

using the cyclic property of the matrix trace, where

$$\mathbf{K} = (\mathbf{F}^\dagger \cdot \Phi \cdot \mathbf{F} \cdot \Psi) \cdot \tilde{\mathbf{R}} - \tilde{\mathbf{R}}^T \cdot (\mathbf{F}^\dagger \cdot \Phi \cdot \mathbf{F} \cdot \Psi)^T. \quad (3.14)$$

From [53], the Wirtinger gradients for Ψ and Φ are then:

$$\frac{\partial}{\partial \bar{\Phi}} = \left(\mathbf{F} \cdot \mathbf{K} \cdot \tilde{\mathbf{R}}^\dagger \cdot \bar{\Psi} \cdot \mathbf{F}^\dagger \right)^T - \left(\bar{\mathbf{F}} \cdot \bar{\Psi} \cdot \tilde{\mathbf{R}} \cdot \mathbf{K} \cdot \mathbf{F}^T \right)^T, \quad (3.15)$$

$$\frac{\partial}{\partial \bar{\Psi}} = \left(\mathbf{F}^\dagger \cdot \bar{\Phi} \cdot \mathbf{F} \cdot \mathbf{K} \cdot \tilde{\mathbf{R}}^\dagger \right)^T - \left(\tilde{\mathbf{R}} \cdot \mathbf{K} \cdot \mathbf{F}^T \cdot \bar{\Phi} \cdot \bar{\mathbf{F}} \right)^T. \quad (3.16)$$

Ψ and Φ are initialized as identity matrices, and stepped iteratively according to these gradients as

$$\Phi_{k+1} = \text{diag}(\Phi_k - \alpha_{\Phi_k} \cdot \text{diag}(\frac{\partial f}{\partial \Phi_k})) \quad (3.17)$$

$$\Psi_{k+1} = \text{diag}(\Psi_k - \alpha_{\Psi_k} \cdot \text{diag}(\frac{\partial f}{\partial \Psi_k})), \quad (3.18)$$

where $\alpha_{\Phi_k} = \frac{\|\frac{\partial f}{\partial \Phi_k}\|^2}{10}$, $\alpha_{\Psi_k} = \frac{\|\frac{\partial f}{\partial \Psi_k}\|^2}{10}$ are the adaptively calculated step sizes at each iteration. The diag operation retains only the components consistent with the assumed ansatz; in Ψ , this corresponds to preserving the diagonal part of each polarization sub-block, whereas for Φ , only the diagonal of the full matrix is preserved.

Results on Experimentally Measured Matrices

The proposed method was first applied to a measured MMF $\mathbf{T}_{2\times}$, in which 38.7% of the total power originally resided in the antisymmetric component. Following optimization, this was reduced to 1.98%. Across multiple trials, the procedure consistently reduced antisymmetric power from 35–45% to below 2% within 10 seconds. In a second experiment, the proximal MMF facet was replaced with a white, plastic eraser—serving as a crude scattering slab—and its RM was measured using an otherwise identical optical setup. In this configuration, the antisymmetric power was reduced from 22.7% to 12.2%. The comparatively poorer performance on the scattering slab was hypothesized to be attributed to the high dynamic range of the sample, leading to limited measurement sensitivity and higher impact of noise. The recovered phase profiles for both samples are shown in Fig. 3.3, and show visual similarity, suggesting recovery of medium-independent aberrations. The spatially linear phase profile exhibited can be primarily interpreted as tilt in the experimental system.

To evaluate the physical plausibility of the corrected scattering matrices, they were additionally examined for agreement with Maxwellian time-reversal symmetry. This principle dictates that a wave retracing its original trajectory—after complex conjugation of its wavefront—should exactly undo the effects of scattering [9]. Thus, for symmetric scattering operators defined over a common input–output spatial basis, applying the complex-conjugated output field associated with an input focal spot results in refocusing at the original illumination location. Constructing the composite operators $\mathbf{R} \cdot \overline{\mathbf{R}}$ and $\mathbf{T}_{2\times} \cdot \overline{\mathbf{T}_{2\times}}$ corresponds to modeling this retro-propagation process simultaneously for all output fields and thus assesses both transpose-symmetry and time-reversibility. Direct conjugation of the operator, instead of the Hermitian, is valid because the input and output bases are expected to be the same in a symmetric operator; that is, $\mathbf{T}^\dagger = \overline{\mathbf{T}}$. As shown in Fig. 1, reshaping a column of the resulting matrix into the illumination mode basis yields the field distribution that would be observed if the conjugated output were backpropagated through the system.

Alternative Formulation of Optimization Problem

To decouple the polarization-rotation effects from spatial aberrations, the near-field composite operator Φ was rewritten as a product of a spatially invariant Jones matrix \mathbf{C}' , containing

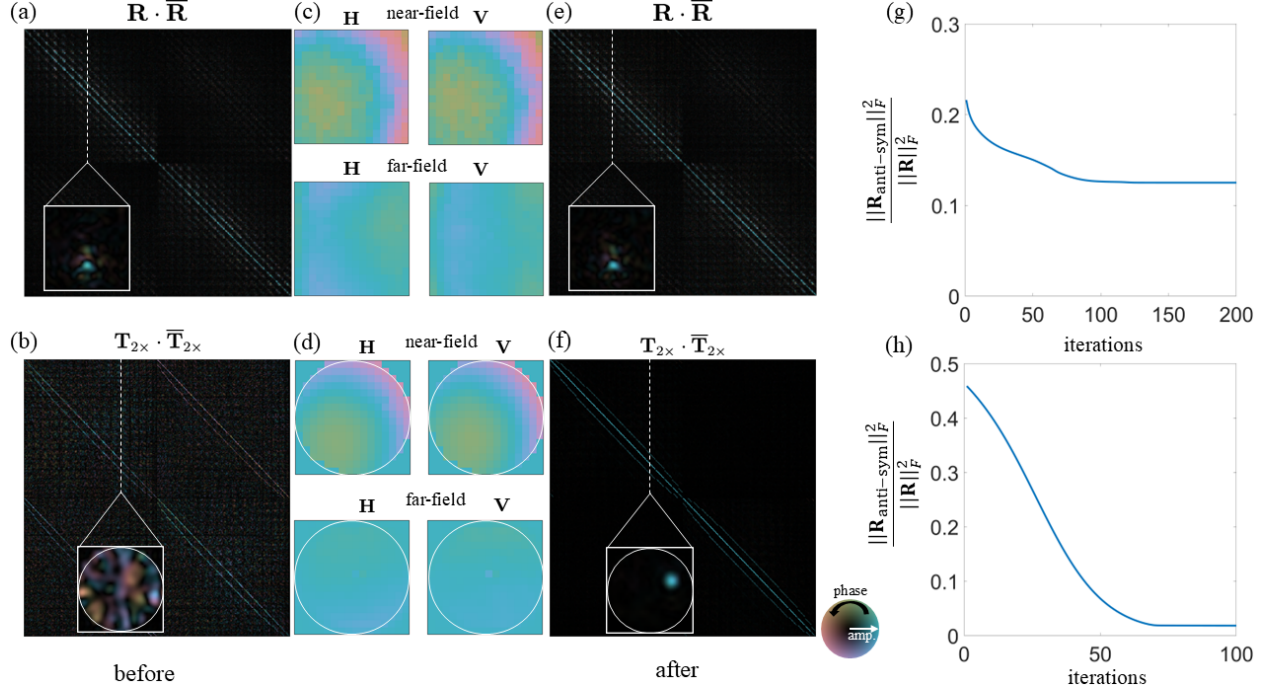


Figure 3.3: Results of reciprocity-based compensation of double-pass MMF TM (bottom row) and slab RM (top row). (a), (b) composite time-reversal operators $\mathbf{R} \cdot \bar{\mathbf{R}}$ and $\mathbf{T}_{2\times} \cdot \bar{\mathbf{T}}_{2\times}$ before correction (c), (d) Recovered near- and far-field phase profiles for both horizontal (H) and vertical (V) polarizations; (e), (f) Corrected operators after optimization, showing restored symmetry and time-reversibility; (g), (h) Normalized Frobenius norm of the antisymmetric component versus iteration.

four unknown complex parameters relevant to describing polarization rotation effects, and a diagonal aberration operator Ψ , which preserved polarization:

$$\begin{bmatrix} \Psi_{HH} & \Psi_{HV} \\ \Psi_{VH} & \Psi_{VV} \end{bmatrix} = \begin{bmatrix} \Psi_H & \mathbf{0} \\ \mathbf{0} & \Psi_V \end{bmatrix} \begin{bmatrix} C'_{11}\mathbf{I} & C'_{12}\mathbf{I} \\ C'_{21}\mathbf{I} & C'_{22}\mathbf{I} \end{bmatrix}, \quad (3.19)$$

where

$$\mathbf{C}' = \begin{bmatrix} C'_{11}\mathbf{I} & C'_{12}\mathbf{I} \\ C'_{21}\mathbf{I} & C'_{22}\mathbf{I} \end{bmatrix} \quad (3.20)$$

and

$$\Psi = \begin{bmatrix} \Psi_H & \mathbf{0} \\ \mathbf{0} & \Psi_V \end{bmatrix}. \quad (3.21)$$

The motivation for this alternative formulation was the hypothesis that the polarization rotation effects could be deduced in closed-form without iteration, given the four complex parameters in \mathbf{C}' and corresponding four Jones sub-blocks in the scattering operators. This was to enhance the computational efficiency of the proposed approach. In the following analysis, the procedure by which this closed-form solution for \mathbf{C}' was derived is shown. The

remaining portion of the compensation operator, consisting of the spatially varying phase terms Φ and Ψ , was optimized as before using gradient descent with Wirtinger derivatives.

In the initial formulation, both near- and far-field terms appeared on the left-hand side of the descent equation, with polarization rotation implicitly embedded in the near-field structure. Upon recognizing that such effects were more plausibly introduced by elements in the illumination optics, \mathbf{C}' was factored to the right-hand side as an equivalent compensatory term \mathbf{C} :

$$\mathbf{C} = \begin{bmatrix} C_{11}\mathbf{I} & C_{12}\mathbf{I} \\ C_{21}\mathbf{I} & C_{22}\mathbf{I} \end{bmatrix} \quad (3.22)$$

The relationship between the right- and left hand-side placement of the correction operator is as follows: if a right hand-side compensatory polarization-rotation term \mathbf{C} is applied to make the measured operator symmetric,

$$\tilde{\mathbf{R}} \cdot \mathbf{C} = \mathbf{C}^T \cdot \tilde{\mathbf{R}}^T, \quad (3.23)$$

left-multiplication by \mathbf{C}^{-T} and right-multiplication by \mathbf{C}^{-1} yields:

$$\mathbf{C}^{-T} \cdot \tilde{\mathbf{R}} = \tilde{\mathbf{R}}^T \cdot \mathbf{C}^{-1}. \quad (3.24)$$

That is, an equivalent transpose-symmetry could be achieved by left-multiplication with \mathbf{C}^{-T} . Hence, the right and left-hand side compensatory terms are transpose-inverses of each other, i.e., $\mathbf{C}' = \mathbf{C}^{-T}$. Without loss of generality, the present formulation adopted the convention in which polarization correction is applied in the illumination path, consistent with the known physical geometry of the experimental system; however, it is not the only valid one.

To compensate polarization effects the measured operator, an optimization problem was again formulated to penalize deviation from transpose-symmetry:

$$\mathbf{R} = \operatorname{argmin} \|\mathbf{R} - \mathbf{R}^T\|_F^2 \quad (3.25)$$

$$\equiv \operatorname{argmin} f, \quad (3.26)$$

where the corrected operator $\mathbf{R} = \mathbf{X}_R \cdot \tilde{\mathbf{R}} \cdot \mathbf{C}$. \mathbf{X}_R is composed of the previously defined near-field term, Ψ , and a corresponding far-field term, Φ :

$$\Phi = \begin{bmatrix} \Phi_H & \mathbf{0} \\ \mathbf{0} & \Phi_V \end{bmatrix}. \quad (3.27)$$

The polarization-corrected operator is expressed as:

$$\tilde{\mathbf{R}} \cdot \mathbf{C} = \begin{bmatrix} \tilde{\mathbf{R}}_{11} & \tilde{\mathbf{R}}_{12} \\ \tilde{\mathbf{R}}_{21} & \tilde{\mathbf{R}}_{22} \end{bmatrix} \begin{bmatrix} C_{11}\mathbf{I} & C_{12}\mathbf{I} \\ C_{21}\mathbf{I} & C_{22}\mathbf{I} \end{bmatrix} = \begin{bmatrix} C_{11}\tilde{\mathbf{R}}_{11} + C_{21}\tilde{\mathbf{R}}_{12} & C_{12}\tilde{\mathbf{R}}_{11} + C_{22}\tilde{\mathbf{R}}_{12} \\ C_{11}\tilde{\mathbf{R}}_{21} + C_{21}\tilde{\mathbf{R}}_{22} & C_{12}\tilde{\mathbf{R}}_{21} + C_{22}\tilde{\mathbf{R}}_{22} \end{bmatrix}. \quad (3.28)$$

Defining

$$\mathbf{E} = \begin{bmatrix} C_{11}\tilde{\mathbf{R}}_{11} + C_{21}\tilde{\mathbf{R}}_{12} & C_{12}\tilde{\mathbf{R}}_{11} + C_{22}\tilde{\mathbf{R}}_{12} \\ C_{11}\tilde{\mathbf{R}}_{21} + C_{21}\tilde{\mathbf{R}}_{22} & C_{12}\tilde{\mathbf{R}}_{21} + C_{22}\tilde{\mathbf{R}}_{22} \end{bmatrix} - \begin{bmatrix} C_{11}\tilde{\mathbf{R}}_{11} + C_{21}\tilde{\mathbf{R}}_{12} & C_{12}\tilde{\mathbf{R}}_{11} + C_{22}\tilde{\mathbf{R}}_{12} \\ C_{11}\tilde{\mathbf{R}}_{21} + C_{21}\tilde{\mathbf{R}}_{22} & C_{12}\tilde{\mathbf{R}}_{21} + C_{22}\tilde{\mathbf{R}}_{22} \end{bmatrix}^T, \quad (3.29)$$

the optimization problem becomes

$$\mathbf{C} = \arg \min \|\mathbf{E}\|_F^2. \quad (3.30)$$

To facilitate the analysis, the squared Frobenius norm was decomposed into contributions from the individual polarization blocks. Specifically, the error terms were grouped into ϵ_1 and ϵ_2 , corresponding to the on-diagonal blocks, and ϵ_3 , which encapsulated the error contribution from off-diagonal blocks:

$$\epsilon_1 = \|C_{11}\tilde{\mathbf{R}}_{11} + C_{21}\tilde{\mathbf{R}}_{12} - C_{11}\tilde{\mathbf{R}}_{11}^T - C_{21}\tilde{\mathbf{R}}_{12}^T\|_F^2, \quad (3.31)$$

$$\epsilon_2 = \|C_{12}\tilde{\mathbf{R}}_{21} + C_{22}\tilde{\mathbf{R}}_{22} - C_{12}\tilde{\mathbf{R}}_{21}^T - C_{22}\tilde{\mathbf{R}}_{22}^T\|_F^2, \quad (3.32)$$

$$\epsilon_3 = 2\|C_{12}\tilde{\mathbf{R}}_{11} + C_{22}\tilde{\mathbf{R}}_{12} - C_{11}\tilde{\mathbf{R}}_{21}^T - C_{21}\tilde{\mathbf{R}}_{22}^T\|_F^2. \quad (3.33)$$

This quantity may be expressed as a quadratic form:

$$\epsilon = \vec{\mathbf{c}}^\dagger \cdot \left(\mathbf{F}_1 \cdot \mathbf{F}_1^\dagger + \mathbf{F}_2 \cdot \mathbf{F}_2^\dagger + \mathbf{F}_3 \cdot \mathbf{F}_3^\dagger \right) \cdot \vec{\mathbf{c}} \equiv \vec{\mathbf{c}}^\dagger \cdot \mathbf{H} \cdot \vec{\mathbf{c}}, \quad (3.34)$$

where the Hermitian matrix

$$\mathbf{H} = \mathbf{F}_1 \cdot \mathbf{F}_1^\dagger + \mathbf{F}_2 \cdot \mathbf{F}_2^\dagger + \mathbf{F}_3 \cdot \mathbf{F}_3^\dagger, \quad (3.35)$$

and

$$\vec{\mathbf{c}} = \vec{\mathbf{C}}, \quad (3.36)$$

$$\mathbf{F}_1 = \begin{bmatrix} \vec{\mathbf{R}}_{11}^\dagger - \vec{\mathbf{R}}_{11} & \vec{\mathbf{R}}_{12}^\dagger - \vec{\mathbf{R}}_{12} & \mathbf{0} & \mathbf{0} \end{bmatrix}^T, \quad (3.37)$$

$$\mathbf{F}_2 = \begin{bmatrix} \mathbf{0} & \mathbf{0} & \vec{\mathbf{R}}_{21}^\dagger - \vec{\mathbf{R}}_{21} & \vec{\mathbf{R}}_{22}^\dagger - \vec{\mathbf{R}}_{22} \end{bmatrix}^T, \quad (3.38)$$

$$\mathbf{F}_3 = \begin{bmatrix} \vec{\mathbf{R}}_{21}^\dagger & \vec{\mathbf{R}}_{22}^\dagger & -\vec{\mathbf{R}}_{11} & -\vec{\mathbf{R}}_{12} \end{bmatrix}^T. \quad (3.39)$$

The arrow superscript denotes column-first vectorization of a matrix.

The error ϵ is a Rayleigh quotient of \mathbf{H} ; so, the optimal \mathbf{C} is attained by the singular vector corresponding to the smallest singular value of \mathbf{H} . The left-hand side phase operator, \mathbf{X}_R , was optimized iteratively using the gradient descent formulation described previously. Since polarization rotation was captured entirely by \mathbf{C} , the near- and far- field terms, Φ and Ψ , were enforced to be purely diagonal at each iteration. During the optimization procedure, an optimal \mathbf{C} was applied every few iterations. However, it was observed that in most cases, much of the polarization rotation was compensated by the first application of \mathbf{C} .

3.3.3 Correction of Single-Pass MMF TMs

Correction of the measured single-pass MMF TMs, $\tilde{\mathbf{T}}_{\text{fw}}$, was subsequently done by enforcing consistency with the symmetry implied by the corrected double-pass operator, $\mathbf{T}_{2\times}$. A correction matrix of the same form, $\mathbf{X}_{\text{fw}} = \mathbf{F}^\dagger \cdot \Phi \cdot \mathbf{F} \cdot \Psi$, was applied on the left-hand

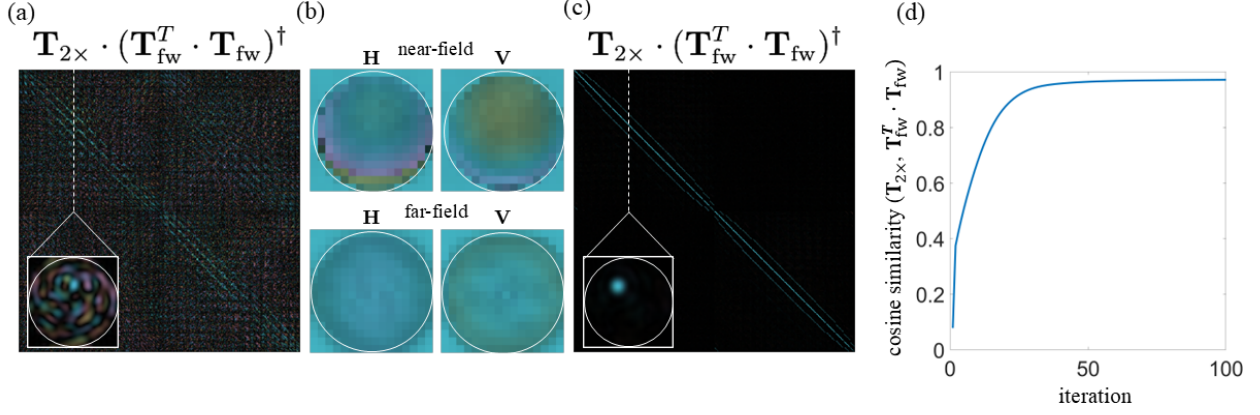


Figure 3.4: Reciprocity-based correction of a single-pass MMF TM. (a) Phase conjugation using the uncorrected single-pass matrix, \mathbf{T}_{fw} , fails to exhibit time-reversibility with the corrected double-pass matrix $\mathbf{T}_{2\times} \cdot (\mathbf{T}_{\text{fw}}^T \cdot \mathbf{T}_{\text{fw}})^\dagger$; (b) Near- and far-field compensatory phase profiles recovered from orthogonal polarization states (H, V) by the proposed method (c) Following optimization, phase conjugation with the corrected single-pass and double-pass operators reconstructs a sharply localized input spot. (d) Convergence of the cosine similarity between the evolving transpose-product $\mathbf{T}_{\text{fw}}^T \cdot \mathbf{T}_{\text{fw}}$ and the target double-pass operator $\mathbf{T}_{2\times}$.

side of $\tilde{\mathbf{T}}_{\text{fw}}$. An optimization problem was then formulated to penalize deviation from the reciprocity-imposed condition $\mathbf{T}_{2\times} = \mathbf{T}_{\text{fw}}^T \cdot \mathbf{T}_{\text{fw}}$:

$$\mathbf{T}_{\text{fw}} = \operatorname{argmin} \|\mathbf{T}_{2\times} - \tilde{\mathbf{T}}_{\text{fw}}^T \cdot \mathbf{X}_{\text{fw}}^T \cdot \mathbf{X}_{\text{fw}} \cdot \tilde{\mathbf{T}}_{\text{fw}}\|_F^2 \equiv \operatorname{argmin} g, \quad (3.40)$$

where the corrected single-pass TM $\mathbf{T}_{\text{fw}} = \mathbf{X}_{\text{fw}} \cdot \tilde{\mathbf{T}}_{\text{fw}}$. Using the matrix trace, g can be expressed as

$$g = \operatorname{tr} \left[\left(\mathbf{T}_{2\times} - \tilde{\mathbf{T}}_{\text{fw}}^T \cdot (\mathbf{F}^\dagger \cdot \Phi \cdot \mathbf{F} \cdot \Psi)^T \cdot \mathbf{F}^\dagger \cdot \Phi \cdot \mathbf{F} \cdot \Psi \cdot \tilde{\mathbf{T}}_{\text{fw}} \right)^\dagger \cdot \left(\mathbf{T}_{2\times} - \tilde{\mathbf{T}}_{\text{fw}}^T \cdot \mathbf{X}_{\text{fw}}^T \cdot \mathbf{X}_{\text{fw}} \cdot \tilde{\mathbf{T}}_{\text{fw}} \right) \right]. \quad (3.41)$$

Substituting $\mathbf{M} = \mathbf{T}_{2\times} - \tilde{\mathbf{T}}_{\text{fw}}^T \cdot \mathbf{X}_{\text{fw}}^T \cdot \mathbf{X}_{\text{fw}} \cdot \tilde{\mathbf{T}}_{\text{fw}}$, the gradients for Φ and Ψ are [53]:

$$\begin{aligned} \nabla_{\Psi} &= \left(\tilde{\mathbf{T}}_{\text{fw}} \cdot \mathbf{M} \cdot \mathbf{T}_{\text{fw}}^\dagger \right)^T \cdot \bar{\Psi} \cdot (\mathbf{F}^\dagger \cdot \bar{\Phi} \cdot \mathbf{F} \cdot \mathbf{F} \cdot \bar{\Phi} \cdot \mathbf{F}^\dagger)^T \\ &\quad + (\mathbf{F}^\dagger \cdot \bar{\Phi} \cdot \mathbf{F} \cdot \mathbf{F} \cdot \bar{\Phi} \cdot \mathbf{F}^\dagger)^T \cdot \bar{\Psi} \cdot \left(\tilde{\mathbf{T}}_{\text{fw}} \cdot \mathbf{M} \cdot \mathbf{T}_{\text{fw}}^\dagger \right)^T, \end{aligned} \quad (3.42)$$

$$\begin{aligned} \nabla_{\Phi} &= \left(\mathbf{F}^\dagger \cdot \bar{\Psi} \cdot \bar{\mathbf{T}}_{\text{fw}} \cdot \mathbf{M} \cdot \mathbf{T}_{\text{fw}}^\dagger \cdot \bar{\Psi} \cdot \mathbf{F}^\dagger \right)^T \cdot \bar{\Phi} \cdot (\mathbf{F} \cdot \mathbf{F})^T \\ &\quad + (\mathbf{F} \cdot \mathbf{F})^T \cdot \bar{\Phi} \cdot \left(\mathbf{F}^\dagger \cdot \bar{\Psi} \cdot \bar{\mathbf{T}}_{\text{fw}} \cdot \mathbf{M} \cdot \mathbf{T}_{\text{fw}}^\dagger \cdot \bar{\Psi} \cdot \mathbf{F}^\dagger \right)^T. \end{aligned} \quad (3.43)$$

As in the symmetric case, Ψ and Φ are initialized as identity matrices and stepped iteratively. At each step, only the diagonal portion of Ψ and Φ is kept, ensuring the preservation of the

ansatz structure:

$$\mathbf{\Phi}_{k+1} = \text{diag}(\mathbf{\Phi}_k - \alpha \cdot \text{diag}(\frac{\partial f}{\partial \mathbf{\Phi}_k})), \quad (3.44)$$

$$\mathbf{\Psi}_{k+1} = \text{diag}(\mathbf{\Psi}_k - \alpha \cdot \text{diag}(\frac{\partial f}{\partial \mathbf{\Psi}_k})). \quad (3.45)$$

This procedure substantially improved alignment between single- and double-pass matrices, as shown in Fig. 3.4. The initial cosine similarity between $\mathbf{T}_{\text{fw}}^T \cdot \mathbf{T}_{\text{fw}}$ and $\mathbf{T}_{2\times}$ was 7.33%, which increased to 97.2% after optimization. In similar fashion to the correction of symmetric operators, time-reversal symmetry was assessed by examining the composite operator $\mathbf{T}_{2\times} \cdot (\mathbf{T}_{\text{fw}}^T \cdot \mathbf{T}_{\text{fw}})^\dagger$. This operator evaluates whether energy sent in round-trip through the MMF can be returned and refocused by time-reversing the forward trajectory. Reshaping a single column to the input basis illustrates the recovery of a single chosen illumination mode.

Chapter 4

Normality in Scattering Operators

4.1 Normal Matrices

4.1.1 Definition and Properties of Normal Matrices

A square matrix $\mathbf{A} \in \mathbb{C}^{n \times n}$ is said to be normal if it commutes with its adjoint [36]:

$$\mathbf{A} \cdot \mathbf{A}^\dagger = \mathbf{A}^\dagger \cdot \mathbf{A}. \quad (4.1)$$

Normal matrices admit diagonalization by a unitary operator, \mathbf{P} :

$$\mathbf{A} = \mathbf{P} \cdot \mathbf{\Lambda} \cdot \mathbf{P}^\dagger, \quad (4.2)$$

where \mathbf{P} satisfies $\mathbf{P} \cdot \mathbf{P}^\dagger = \mathbf{P}^\dagger \cdot \mathbf{P} = \mathbf{I}_n$ and \mathbf{P} has orthonormal columns corresponding to the eigenvectors of \mathbf{A} ; $\mathbf{\Lambda}$ is a diagonal matrix that contains the associated eigenvalues [36]. Furthermore, since the same orthonormal basis spans both the domain and codomain of the matrix, the singular values of a normal matrix are simply the absolute values of its eigenvalues; this is not generally the case [36]. In some sense, normality thus generalizes unitarity, which imposes the stricter demand on phase-only eigenvalues; both unitary and normal matrices carry energy through their orthonormal eigenbases, but unitary operators do so without loss. The energy in a normal operator is captured entirely by the energy contained in its eigenvalues [36]:

$$\|\mathbf{A}\|_F^2 = \sum_{i=1}^n |\lambda_i|^2, \quad (4.3)$$

where λ_i are the eigenvalues of \mathbf{A} . A normal matrix, being diagonalizable, is necessarily of full rank and hence invertible. Owing to the orthogonality of its eigenbasis, however, such a matrix exhibits spectral characteristics distinct from those of other full-rank matrices. The relevant properties are discussed in the following sections.

4.1.2 Spectra and Pseudospectra of Normal Matrices

The set of all eigenvalues of a matrix $\mathbf{A} \in \mathbb{C}^{n \times n}$ is denoted by $\sigma(\mathbf{A})$ and referred to as its spectrum. For a normal matrix, or one in proximity to normality, as will be defined precisely,

perturbations to \mathbf{A} produce only minor displacements in the spectrum [54]. This stability reflects the orthogonality of the eigenvectors: a perturbation of one vector leaves it well separated from the others, preserving the integrity of the eigenspace. Conversely, when the eigenvectors approach linear dependence, a perturbation may drive them into degeneracy, thereby reducing the rank and rendering the matrix non-invertible. These ideas are formalized through the concepts of spectra and pseudospectra of operators.

The analysis proceeds by relaxing the definition of an eigenvector in order to characterize the sensitivity of the spectrum. An eigenvalue λ_i of \mathbf{A} is identified by the singularity of $\mathbf{A} - \lambda_i \mathbf{I}_n$ [54]. The ϵ -pseudospectrum is obtained when strict singularity is replaced by the requirement that the condition number of $\mathbf{A} - \lambda \mathbf{I}_n$ exceed a prescribed threshold, thereby defining the set of complex numbers for which the norm of the inverse is sufficiently large [54]:

$$\sigma_\epsilon(\mathbf{A}) = \left\{ z : z \in \mathbb{C}, \left\| (\mathbf{A} - z \mathbf{I}_n)^{-1} \right\|_2 > \frac{1}{\epsilon} \right\}, \quad (4.4)$$

where $\left\| (\mathbf{A} - \lambda_i \mathbf{I}_n)^{-1} \right\|_2$ is called the resolvent norm, and the 2-norm $\| \cdot \|_2$ refers to the largest singular value of a matrix [54]. It is somewhat assumed here that $\| \mathbf{A} \|_2$ is close to unity, so as to make the resolvent norm meaningful in comparison. For a normal matrix,

$$\left\| (\mathbf{A} - \lambda_i \mathbf{I}_n)^{-1} \right\|_2 = \left\| (\mathbf{P} \cdot \mathbf{\Lambda} \cdot \mathbf{P}^\dagger - z \mathbf{I}_n)^{-1} \right\|_2 \quad (4.5)$$

$$= \left\| \mathbf{P} \cdot (\mathbf{\Lambda} - z \mathbf{I}_n)^{-1} \cdot \mathbf{P}^\dagger \right\|_2 \quad (4.6)$$

$$= \left\| (\mathbf{\Lambda} - z \mathbf{I}_n)^{-1} \right\|_2 \quad (4.7)$$

$$\equiv \max_i \frac{1}{|\lambda_i - z|}, \quad (4.8)$$

where the norm-invariance of the unitary operator \mathbf{P} allows the simplification from the third to the fourth step. The resolvent norm decays inversely with the distance from the spectrum, so the ϵ -pseudospectra of a normal matrix form an ϵ -neighborhood around the eigenvalues. In the non-normal case, the pseudospectra can deviate substantially from the eigenvalue distribution, due to the effect of eigenvector non-orthogonality [54]. Even small perturbations may cause large spectral shifts, and the pseudospectral contours can extend far from the spectrum, producing lobes or elongated regions absent in normal matrices [54]. This often arises when clusters of near-zero eigenvalues coexist with a large operator norm, signaling spectral instability and the loss of orthogonality in the eigenbasis. The diagonalizing operator for a non-normal matrix is not unitary and therefore does not preserve the norm. For example, consider a non-normal diagonalizable matrix $\mathbf{B} = \mathbf{U} \cdot \mathbf{L} \cdot \mathbf{U}^{-1}$. Following an analysis similar to that above shows that the resolvent norm of \mathbf{B} depends on both $\left\| (\mathbf{L} - z \mathbf{I}_n)^{-1} \right\|_2$ and $\kappa(\mathbf{U})$, the condition number of the diagonalizing operator. Since no direct spectral bound exists for \mathbf{U} in the general case, this condition number can be arbitrarily large; therefore, pseudospectra of non-normal matrices can vary unpredictably in response to changes in the spectrum [54].

Closely related is the field of values, also known as the numerical range, defined as the set of all quadratic forms $\mathbf{x}^\dagger \mathbf{A} \mathbf{x}$ where $\| \mathbf{x} \| = 1$. This set is always convex and contains the spectrum of \mathbf{A} [54]. For normal matrices, the pseudospectra remain tightly clustered around the eigenvalues, with level sets forming concentric or nearly circular contours [54]. The field of values tends to coincide with or closely enclose the convex hull of the eigenvalues, particularly in the Hermitian case.

The natural question of how to assess the normality of a matrix arises in this context. Henrici [37] defines the departure from normality as

$$\epsilon(\mathbf{A}) = \sqrt{\|\mathbf{A}\|_F^2 - \sum_i |\lambda_i|^2}, \quad (4.9)$$

where $\mathbf{A} \in \mathbb{C}^{n \times n}$ is a diagonalizable matrix and λ_i are its eigenvalues. This expression compares the Frobenius norm of the matrix, which depends on all entries, to the ℓ_2 -norm of its spectrum, which for a normal matrix would be equal by the spectral theorem [36]. If \mathbf{A} is exactly normal, the two terms are identical and $\epsilon(\mathbf{A})$ vanishes. Nonzero values therefore measure the excess Frobenius norm unaccounted for by the eigenvalues alone, which arises from the non-orthogonality of the eigenvectors. In this sense, $\epsilon(\mathbf{A})$ captures how far the matrix is from having a unitary diagonalizing transformation, with larger values indicating stronger deviations from normal behavior [37]. The departure from normality has several interesting consequences with regard to matrix operations. For example, Henrici showed that the departure directly bounds the norm of the powers of matrices and fields of values [37], and Descloux extended these bounds to a larger class of functions [55].

The spectral theory described briefly here provides a mathematically rigorous framework to characterize regimes of transport in complex media. The following sections cover the details of the experimental and theoretical investigation conducted to apply these insights to transmission and reflection matrices of complex media.

4.2 Normality of Transmission and Reflection Matrices

4.2.1 Green's Function and Stratton-Chu Boundary Field Integrals

The scattering matrix of an optical system is a mapping between a chosen set of input and output energy-carrying modes [9, 10]. Underlying this linear relationship is the continuous-space Green's operator (or Green's function), which arises from the linearity of time-harmonic Maxwell's equations. As covered in Chapter 2, if a scalar field $U_\omega^i(\mathbf{r})$ is incident on an inhomogeneous volume V , the resulting scattered field $U_\omega(\mathbf{r})$ is given by

$$U_\omega(\mathbf{r}) = U_\omega^i(\mathbf{r}) + \int_V F_\omega(\mathbf{r}') U_\omega(\mathbf{r}') \mathbf{G}_\omega(\mathbf{r}, \mathbf{r}') d^3r', \quad (4.10)$$

where $F_\omega(\mathbf{r}) = \frac{1}{4\pi} k^2 (n_\omega^2(\mathbf{r}) - 1)$ is the scattering potential of the medium described by its refractive index $n(\mathbf{r})$ and the wavenumber k , and $\mathbf{G}_\omega(\mathbf{r}, \mathbf{r}')$ is a Green's function of the Helmholtz operator:

$$\nabla^2 \mathbf{G}_\omega(\mathbf{r}) + \left(\frac{\omega^2}{c^2} \right) \epsilon_\omega(\mathbf{r}) \mathbf{G}_\omega(\mathbf{r}) = \delta^3(\mathbf{r} - \mathbf{r}') \mathbf{1}, \quad (4.11)$$

where $\delta^3(\mathbf{r} - \mathbf{r}') \mathbf{1}$ is the Dirac delta tensor. When the background is taken as free space, \mathbf{G}_ω is the free-space Green's function and F_ω encodes the full inhomogeneity; but one may also choose a more structured background (e.g., a waveguide), in which case F_ω represents only

the residual contrast. Nevertheless, the convolution integral conveys a superposition of field responses dictated by the Green’s function and scattering potential, which together define the inhomogeneity encountered by the incident field.

The Stratton–Chu formulation [56] recasts the scattering problem by expressing the fields external to an inhomogeneous region solely in terms of equivalent surface currents on its boundary. This approach transforms the volume integral inherent in the integral equation for scattering into a surface integral involving the Green’s function of the chosen background medium. Consequently, the boundary fields may be expanded in the orthonormal modal basis of the waveguide, enabling propagation described by the modal Green’s function. Thus, the scattering process is elegantly reduced to modal amplitude evolution governed by surface interactions, avoiding explicit volumetric computations. Since the Stratton–Chu formulation involves only fields on the boundary, it naturally yields a formalism close to that of the scattering matrix by relating incident and scattered modal amplitudes at the waveguide ports without recourse to the interior field distribution. It provides the natural bridge between the Green’s functions of Lippman-Schwinger scattering theory and those discussed here.

The following section aims to explore the connection between the continuous-space, integral kernel form of the Green’s function and properties of a measured transmission or reflection matrix. The paraxial approximation is used henceforth, in which fields are assumed to vanish in the direction of propagation, z , in a waveguide. Though most aspects of the following discussion have been well-studied in mathematics literature, to the author’s knowledge, they have not been explicitly connected to optical scattering.

4.2.2 Operator-Theoretic and Modal Green’s Function

In the previous section, the response of an optical system to an illumination field was given by convolution with its Green’s function. More generally, this may be expressed in operator form. Let source and response electric fields, $\mathbf{E}_\omega^s(\mathbf{r})$ and $\mathbf{E}_\omega(\mathbf{r})$ belong to a Hilbert space \mathcal{H} under the standard inner product. The response to an illumination field is then given by:

$$\mathbf{E}_\omega(\mathbf{r}) = \mathbf{G}_\omega \cdot \mathbf{E}_\omega^s(\mathbf{r}), \quad (4.12)$$

where \mathbf{G}_ω is the Green’s operator at frequency ω , and the multiplication \cdot is defined in operator space to correspond to convolution. In source-free media, the system action cannot increase energy i.e. $\|\mathbf{G}_\omega \cdot \mathbf{E}_\omega^s(\mathbf{r})\| \leq \|\mathbf{E}_\omega^s\|$. Any physical \mathbf{G} must, therefore, be a bounded operator, and exhibit a decaying singular value spectrum [45].

If the optical system under examination exhibits specific symmetries or geometries, solving the Helmholtz equation may yield a Green’s operator that acts as a modal propagator. That is, its eigenfunctions form a complete orthonormal basis set which diagonalizes the system. \mathbf{G}_ω is a normal operator, and admits unitary diagonalization by these eigenfunctions. Each eigenfunction, or eigenmode, serves as an orthogonal information-carrying channel of the system, and responds independently of the others under propagation. This perspective enables a transition from a general convolutional description to a modal one, because scattering integral can be simplified to a sum of inner products over these eigenmodes.

Here, propagation from one interface of a waveguide is considered, along the propagation axis z . Associated with each eigenmode $\{\psi_i\}_{i=1}^N$ is a propagator $e^{j\beta_i z}$ which encodes the phase

and amplitude evolution corresponding to the real and imaginary parts of β , respectively:

$$\mathbf{G}_\omega \cdot \mathbf{E}_\omega^s = \sum_{i=1}^N \psi_i^\dagger \cdot \langle \psi_i, \mathbf{E}_\omega^s \rangle \cdot e^{j\beta z}, \quad (4.13)$$

where $\langle \cdot | \cdot \rangle$ denotes the inner product such that $\langle \psi_i | \psi_j \rangle = 0 \Leftrightarrow i \neq j$. Conceptually, this means the following: the incident field $\mathbf{E}_\omega^s(\mathbf{r})$ excites a superposition of eigenmodes according to the inner product taken between \mathbf{E}_ω^s and each ψ_i . The system then acts by transforming each mode in phase and amplitude, and the resulting field results from coherent interference among the propagated modes. In the following section, it is shown how this structure becomes manifest in the experimentally measured transmission or reflection matrix, which provides a discretized representation of the Green's function between input and output mode bases.

4.2.3 Compression of the Green's Operator

The Green's operator \mathbf{G}_ω , which governs the response of the system, is an infinite-dimensional linear operator acting on continuous fields. However, any physical measurement or actuation necessarily involves a finite number of degrees of freedom, such as input and output modes sampled by spatial light modulators or detectors. As a result, the monochromatic, coherent transmission matrix \mathbf{T}_ω of an optical system should be understood as a compression of \mathbf{G}_ω ; that is, a finite-dimensional operator obtained by restricting the action of \mathbf{G} to chosen subspaces of inputs and outputs [45].

In functional analysis, compressions of operators are typically defined by restricting both the domain and codomain of a single operator to a subspace, often through orthogonal projection, yielding a smaller operator that captures behavior within that subspace [45]. However, in experimental settings such as transmission matrix measurements, the process is inherently double-sided: the input and output channels are independently defined, and need not span the same subspace or be related by orthogonality. As such, the experimentally measured transmission matrix should be viewed as a bi-compression of the Green's operator—one that projects the input field onto a finite illumination basis (e.g., SLM modes or focal spots) and the output field onto a finite detection basis (e.g., camera pixels or photodetector channels). While traditional compressions aim to approximate an operator's internal dynamics within a subspace, transmission matrices reflect how the operator maps between externally defined bases, and thus encode both the physics of the medium and the choice of how one interrogates it. \mathbf{T}_ω (or simply \mathbf{T}) thus encodes a compression of the infinite-dimensional physics into a pair of experimentally accessible bases corresponding to illumination and measurement:

$$\mathbf{T} = \mathbf{P}_{\text{out}} \mathbf{G}_\omega \mathbf{P}_{\text{in}}, \quad (4.14)$$

where \mathbf{P}_{in} and \mathbf{P}_{out} specify the input (e.g., SLM modes or input focal spots) and output (e.g., camera pixels) bases, respectively, under which the measurement is conducted. The choice of \mathbf{P}_{in} and \mathbf{P}_{out} affects how accurately \mathbf{T} captures the intrinsic transport properties of the medium. In particular, the compression must ensure that the spectral properties of \mathbf{G} are inherited by \mathbf{T} . For \mathbf{T} to remain normal under compression, its domain and co-domain must have the same eigenstructure as \mathbf{G} . In other words, the compression of results in an operator

whose domain and codomain have the same set of eigenvectors of \mathbf{G} , and hence span the same sub-eigenspaces. This corresponds to compression onto a reducing subspace [45]. Moreover, if represents a physical system with a finite number of nonzero singular vectors, then is a compact operator of finite rank. In this case, some number of eigenvectors $n \leq N$ are chosen from the eigenspace of \mathbf{G} , and \mathbf{P}_{in} and \mathbf{P}_{out} are isometries with codomain defined by this sub-eigenspace, $\mathcal{K} \subseteq \mathcal{H}$. \mathcal{K} must then be invariant under \mathbf{G} and its adjoint, \mathbf{G}^\dagger [45]. The compression results in an operator \mathbf{T} whose span is \mathcal{K} . For \mathbf{T} to fully represent the complete modal space spanned by \mathbf{G} , the reducing subspace must be of the same rank as \mathbf{G} itself; that is, $n = N$ and $\mathcal{K} = \mathcal{H}$. Under these conditions, \mathbf{T} retains the spectral structure of \mathbf{G} and remains normal under compression.

Physically, this translates to a requirement that the input and output measurement schemes faithfully and symmetrically represent the system being probed. The illumination basis (e.g., SLM modes) must be properly aligned, scaled, and matched with the detection basis (e.g., camera pixels), such that the physical interface of the system, such as the facet of a MMF, is represented identically on both sides of \mathbf{G} . In the case of an MMF, this means that the domain and codomain of \mathbf{T} must span bases that map onto the same modal system, ensuring that \mathbf{T} accurately captures modal preservation rather than introducing artifacts from misalignment or asymmetric sampling.

In this context, the specifications of detection optics used in an experimental apparatus, such as lenses of finite numerical aperture, impose a constraint on the accessible spatial frequency content of the fields. If the detection optics fail to collect the full angular spectrum supported by the medium, such as the high spatial frequency light reflected from a multiply-scattering slab, then those components are effectively truncated from \mathbf{P}_{out} . As a result, \mathbf{T} ceases to inherit the full modal spectrum of \mathbf{G} , and time-reversibility may be broken by the asymmetry between illumination and collection. In this sense as well, the fidelity of \mathbf{T} as a representation of the underlying operator depends on the experimental aperture through which it is realized.

4.2.4 Experimental Analysis of Normality

The spectral behavior of scattering matrices in complex media was examined through direct measurement of (i) single- and double-pass MMF TMs and (i) scattering slab RMs. These measurements provide a means to assess whether the observed operators exhibit properties consistent with normal or nearly normal behavior, as predicted by the operator-theoretic framework introduced above. Normality was quantitatively evaluated using a normalized form of Henrici's departure, which amounts to assessing the fraction of energy accounted for by the eigenvalues:

$$\eta(\mathbf{A}) = \frac{\sum_i |\lambda_i|^2}{\|\mathbf{A}\|_F^2}, \quad (4.15)$$

where $\mathbf{A} \in \mathbb{C}^{n \times n}$ is a diagonalizable $n \times n$ complex matrix whose eigenvalues are λ_i .

First, MMF TMs were examined for normality. The experimentally measured matrices, \mathbf{T}_{fw} and $\mathbf{T}_{2 \times}$ were acquired in a "spot-to-pixel" basis, with a 16×16 grid of focal spots used for illumination and a 109×109 output camera pixel grid recorded per polarization

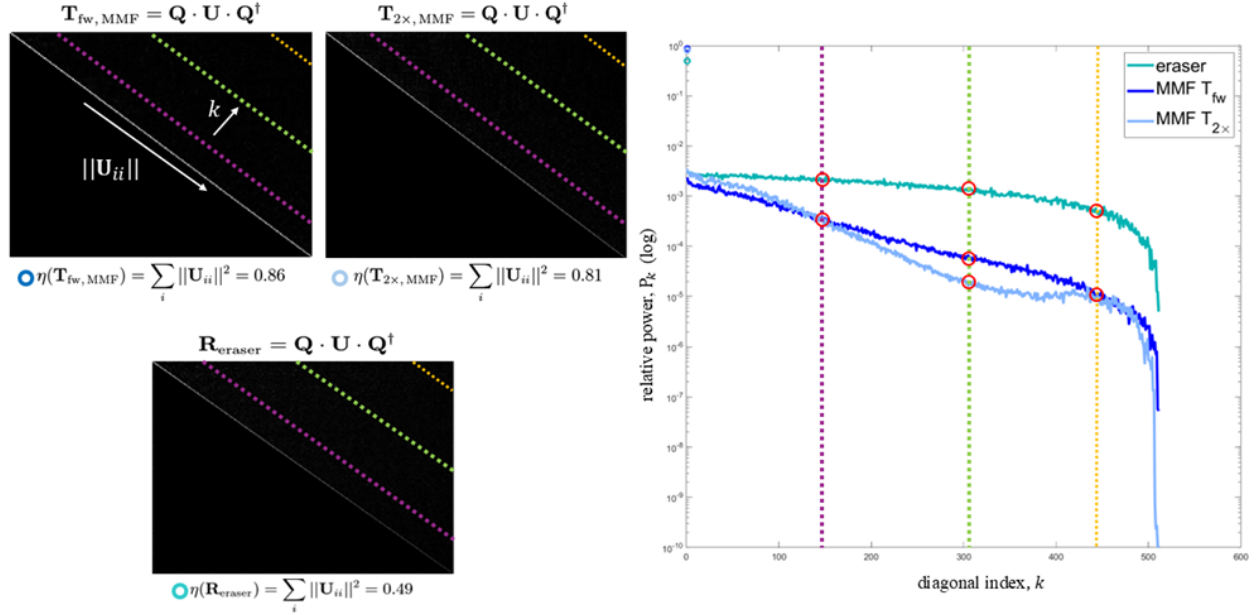


Figure 4.1: Schur decompositions of single-pass (\mathbf{T}_{fw}), double-pass ($\mathbf{T}_{2\times}$) MMF TMs and eraser RMs (\mathbf{R}). Off diagonal energy decays strongly (select sub-diagonals illustrated by purple, green, and orange lines) for non-normal eraser RM compared to MMF TMs, suggesting mode orthonormality present in structured waveguides like MMF but not general scattering media.

channel, yielding matrices of size 23762×512 . To evaluate spectral energy, the TMs were converted to a square form by resampling the output. The recorded holograms on the pixel grid were spatially cropped to a 16×16 region in the spatial frequency domain. An inverse Fourier transform was then applied, yielding a 512×512 matrix mapping input spots to a sub-sampled output basis. This resampling is justified because the fiber's numerical aperture (NA) limits the maximum spatial frequency that can be supported at the output. As a result, the high-frequency components beyond the NA cutoff, though recorded by the camera, carry negligible energy and do not contribute to the meaningful modal content. In conceptual terms, this is to say that the speckle pattern of the MMF does not vary meaningful with respect to the spatial frequency defined by the size of one or even a few consecutive camera pixels. By truncating in the Fourier domain to the NA-limited region, we preserve all physically relevant information while reducing the output basis to match the input dimensionality.

Though square, these TMs were still expressed in an asymmetric basis, with input defined over focal spots and output over camera pixels. To register the spatial coordinates between these domains, the input spot grid was directly imaged onto the camera by removing the MMF facet and replacing it with a reflector. The pixel coordinates corresponding to the centers of each illumination spot were recorded, and the average point-spread function of the spots was fitted to a Gaussian profile with a total width of approximately 11×11 pixels. A basis transformation matrix between the spot and pixel grids, $\mathbf{U}_{\text{pixel-to-spot}}$,

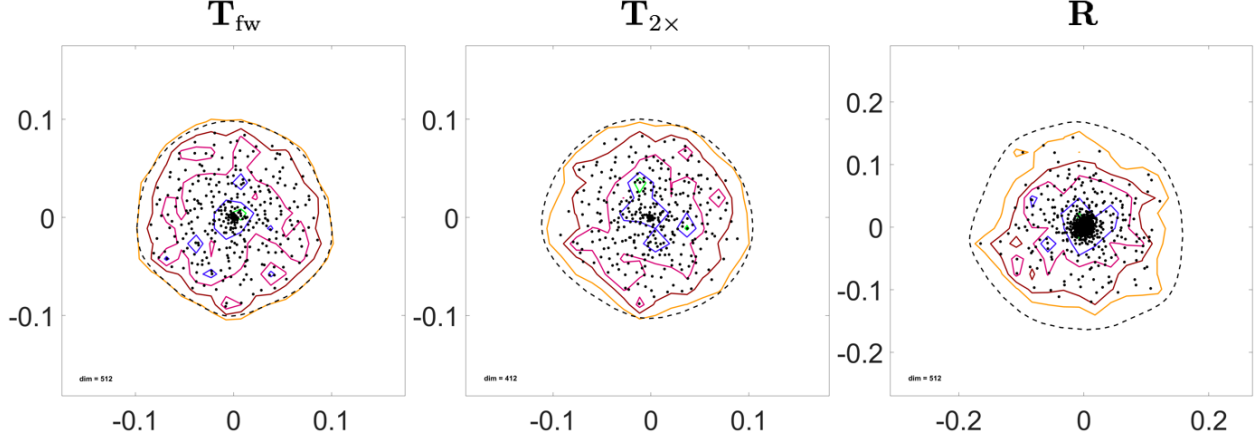


Figure 4.2: Spectra, pseudospectra, and fields of values of single-pass (\mathbf{T}_{fw}), double-pass (\mathbf{T}_{2x}) MMF TMs and an eraser (\mathbf{R}). The relatively smooth, circular pseudospectral contours of the MMF TMs suggest spectrally stable transport regimes, as opposed to their bloated counterparts in the slab RM.

was constructed by vectorizing the superposition of pixels corresponding to each spot and subsampling the resulting matrix of pixels in the Fourier domain to a 16×16 grid, as described previously. Since each spot was modeled as an orthogonal spatial basis function, $\mathbf{U}_{\text{pixel-to-spot}}$ is a partial isometry with orthonormal columns up to the rank of the number of spots, i.e., 256. $\mathbf{U}_{\text{pixel-to-spot}}^\dagger$ was then basis transformation matrix between spot and pixel basis representations. For full, polarization-resolved conversion, $\mathbf{U}_{\text{pixel-to-spot}}^\dagger$ was applied along each polarization state:

$$\mathbf{U} = \begin{bmatrix} \mathbf{U}_{\text{pixel-to-spot}}^\dagger & \mathbf{0} \\ \mathbf{0} & \mathbf{U}_{\text{pixel-to-spot}}^\dagger \end{bmatrix}. \quad (4.16)$$

Hence, right multiplication of the subsampled \mathbf{T} by \mathbf{U} corresponds to conversion from the spot basis to the subsampled-pixel basis on the input side. After registration, the single-pass TM exhibited $\eta(\mathbf{T}_{fw}) = 88.2\%$ and the corresponding double-pass, $\eta(\mathbf{T}_{2x}) = 82.8\%$. exhibited RMs of a scattering slab, denoted \mathbf{R} , were then examined for normality. In accordance to low modal transport, $\eta(\mathbf{R}) = 49.3\%$ after spatial registration.

To visualize the spectral structure of the scattering matrix, a Schur decomposition was computed and plotted in Fig. 4.1. The upper-triangular form highlights the degree of modal coupling. MMF TMs exhibit near-diagonal dominance, while slab RMs display more broadly distributed off-diagonal terms. The normality metric employed in this investigation is the sum of the squares of the diagonals of the Schur matrices. Plotting the log-magnitude of the upper-triangular entries by index further reveals a slower decay in the slab, consistent with non-normal behavior. Color-coded diagonals (purple, green, and orange) are aligned across subplots corresponding to various sub-diagonals of each Schur matrix. These results suggest the interpretation of modal structure as close-to normal and disordered reflection as non-normal.

The pseudospectra of the measured operators was subsequently examined. In Fig. 4.2, the eigenvalues of each operator (single- and double-pass TM, and slab RM) are shown as

black points in the complex plane. Several ϵ -pseudospectra are plotted such that contours further from the origin correspond to larger ϵ . The field of values is plotted as a dashed line. The plots were generated using Eigtool, a freely available software developed by Thomas G. Wright and Nicholas Trefethen at the University of Oxford [57].

In the first panel, the eigenvalues of the single-pass TM form a nearly circular cloud centered near the origin, filling much of the unit disk. The pseudospectra wrap tightly around the eigenvalue distribution, and the field of values closely follows the same boundary. This behavior is characteristic of a nearly normal matrix. Physically, this suggests that the MMF supports a set of nearly orthogonal propagating modes.

The second panel shows the analysis of the double-pass TM. Here the eigenvalue distribution becomes slightly distorted, spreading outward and losing its circular symmetry to a small extent. The pseudospectra balloon and elongate slightly, and the field of values no longer provides as tight of a bound. This indicates a slight breakdown of normality. The resulting operator exhibits mild transient amplification and sensitivity to alignment or phase mismatch.

In the third panel, the plot corresponding to the reflection matrix of a scattering slab is shown. Most eigenvalues collapse toward the origin, with only a sparse scattering beyond. The pseudospectra spread dramatically, forming irregular lobes far from the eigenvalue core, and the field of values takes on a distorted shape. This matrix is strongly non-normal. In such a system, light is reflected diffusely, and the mapping from input to output involves multiple-scattering and disordered paths. The operator is dominated by non-orthogonal projections, and its eigenvalues are of little use in predicting its physical behavior. The resolvent norm grows rapidly with small perturbations, and the matrix does not diagonalize cleanly in any orthonormal basis.

The sequence of panels captures a transition from nearly modal transport, through accumulating mode-mixing, to complete mode non-orthonormality. The single-pass TM behaves as a nearly normal operator with stable spectral characteristics. The double-pass matrix, though derived from the same medium, may indicate the consequences of distal side reflection from an imperfect facet and a longer optical path, resulting in more mode-mixing and thus reduced normality. The reflection matrix, shaped by multiple scattering, stands at the far end of the spectrum, where non-normality dominates and spectral intuition breaks down. This progression underscores the role of normality in determining whether eigenvalues can be trusted to describe the physics of light propagation through complex media.

4.2.5 Normality and Parametric Dispersion Modeling

The preceding discussion concerned the structure of a scattering matrix at a fixed wavelength. In many applications, including depth-resolved imaging and spectrally broadband sensing, it is necessary to predict the operator's behavior across a finite spectral range. This raises the question of how algebraic properties such as normality influence spectral evolution. For a normal operator with wavelength-invariant eigenvectors, the frequency evolution is particularly simple, as the operator and its frequency derivative are then simultaneously diagonalizable. The following develops this connection in detail.

Dispersion Model for Normal Operators

Let $\mathbf{S}(\omega)$ denote the scattering operator, relating an input \vec{x} to an output \vec{y} ,

$$\vec{y} = \mathbf{S}(\omega) \cdot \vec{x}. \quad (4.17)$$

Differentiation with respect to angular frequency gives

$$\frac{\partial \vec{y}}{\partial \omega} = \frac{\partial \mathbf{S}}{\partial \omega} \cdot \vec{x} \quad (4.18)$$

$$= \frac{\partial \mathbf{S}}{\partial \omega} \mathbf{S}^{-1} \cdot \vec{y}, \quad (4.19)$$

a linear ordinary matrix differential equation in ω . The coefficient matrix,

$$\mathbf{s}(\omega) = \frac{\partial \mathbf{S}}{\partial \omega} \mathbf{S}^{-1}, \quad (4.20)$$

is closely related to the Wigner–Smith operator,

$$\mathbf{Q} = -j \mathbf{S}^{-1} \frac{\partial \mathbf{S}}{\partial \omega}, \quad (4.21)$$

whose eigenvalues represent group delays of the input modes [38, 41].

Given $\mathbf{S}(\omega_0)$ at a reference frequency ω_0 , the formal solution of Eq. (4.19) is an initial-value problem, whose solution is given by

$$\mathbf{S}(\omega) = \exp \left(\int_{\omega_0}^{\omega} \mathbf{s}(\omega') d\omega' \right) \mathbf{S}(\omega_0). \quad (4.22)$$

The Magnus expansion [58] expresses the argument of this exponential as an infinite series

$$\Omega(\omega) = \sum_{k=1}^{\infty} \Omega_k(\omega) \quad (4.23)$$

where

$$\Omega_1(\omega) = \int_{\omega_0}^{\omega} \mathbf{s}(\omega_1) d\omega_1, \quad (4.24)$$

$$\Omega_2(\omega) = \frac{1}{2} \int_{\omega_0}^{\omega} d\omega_1 \int_{\omega_0}^{\omega_1} d\omega_2 [\mathbf{s}(\omega_1), \mathbf{s}(\omega_2)], \quad (4.25)$$

...

and

$$\mathbf{S}(\omega) = \exp [\Omega(\omega)] \mathbf{S}(\omega_0). \quad (4.26)$$

Conceptually, the first-order term corresponds to the direct product integral of $\mathbf{s}(\omega)$, with Ω_1 serving as its generator, while higher-order terms provide corrections that account for

the non-commutativity of $\mathbf{S}(\omega)$ at different frequencies. This parametric model reduces the wavelength variation to an expansion in the matrices $\Omega_k(\omega)$.

If $\mathbf{S}(\omega)$ is normal such that $\mathbf{S}(\omega) = \mathbf{P}(\omega) \cdot \mathbf{\Lambda}(\omega) \cdot \mathbf{P}(\omega)^\dagger$, Eq. (4.19) becomes

$$\frac{\partial \vec{y}}{\partial \omega} = \left(\frac{\partial \mathbf{P}}{\partial \omega} \cdot \mathbf{\Lambda} \cdot \mathbf{P}^\dagger + \mathbf{P} \cdot \frac{\partial \mathbf{\Lambda}}{\partial \omega} \cdot \mathbf{P}^\dagger + \mathbf{P} \cdot \mathbf{\Lambda} \cdot \frac{\partial \mathbf{P}^\dagger}{\partial \omega} \right) (\mathbf{P} \cdot \mathbf{\Lambda}^{-1} \cdot \mathbf{P}^\dagger) \cdot \vec{y}. \quad (4.27)$$

Under the simplifying assumption of fixed $\mathbf{P}(\omega)$ (valid in the principal mode basis of multimode waveguides under perturbative wavelength variation, for example [18, 59]) this simplifies to

$$\frac{\partial \vec{y}}{\partial \omega} = \mathbf{P} \cdot \frac{\partial \mathbf{\Lambda}}{\partial \omega} \mathbf{\Lambda}^{-1} \cdot \mathbf{P}^\dagger \cdot \vec{y}. \quad (4.28)$$

In this formalism, the generator is diagonal in the principal-mode basis, and the frequency dependence of the scattering operator reduces to a set of uncoupled, mode-dependent group delays. In this case, \mathbf{Q} is diagonal in the same basis and commutes with $\mathbf{S}(\omega)$ for all ω , so that the Magnus expansion terminates at first order. Given the scattering operator at some frequency ω_0 , estimating it at a nearby frequency $\omega_0 + \Delta\omega$ then reduces to left-multiplication by a correction operator that accumulates modal group delays over the spectral interval:

$$\mathbf{S}(\omega + \Delta\omega) = \mathbf{D}_1(\Delta\omega) \cdot \mathbf{S}(\omega), \quad (4.29)$$

where $\mathbf{D}_1(\Delta\omega) = \mathbf{P} \cdot e^{\mathbf{\Lambda}\Delta\omega} \cdot \mathbf{P}^\dagger$. More generally, $\mathbf{S}(\omega)$ forms a family of matrices in a Lie group, with $\mathbf{s}(\omega)$ in the corresponding Lie algebra. If $[\mathbf{S}(\omega_1), \mathbf{S}(\omega_2)] \neq 0$, as occurs when the eigenvectors vary with ω or the operator is not normal, higher-order commutator terms appear in the Magnus expansion. Physically, this corresponds to modal coupling, represented by off-diagonal elements in $\mathbf{\Lambda}(\omega)$ in the principal-mode basis. Such coupling breaks the simultaneous diagonalizability of \mathbf{S} and \mathbf{Q} , producing nonzero commutators over the spectral interval and necessitating higher-order corrections, as prescribed by the Baker–Campbell–Hausdorff formula [60–66].

It follows that the degree of normality should determine the extent to which a first-order, parametric dispersion model accurately describes the spectral evolution of the scattering operator. The following section examines this relationship for MMFs with varying normality.

Measurement and Fitting of Multi-Spectral MMF Transmission Matrices

To investigate this hypothesis, multi-spectral MMF TMs (msTMs) were measured in two regimes: (1) in the absence of external perturbation, and (2) under static mechanical compression applied by a fiber-optic mode scrambler. The scrambler was expected to increase modal crosstalk and shifts in the eigenbasis and thereby reduce the accuracy of the first-order dispersion model over a given spectral bandwidth. After the spatial registration procedure described in the previous section, the normality $\eta(\mathbf{T})$ of the unscrambled and mode-scrambled MMF TMs were 0.84 and 0.62, respectively, indicating a substantial reduction in spectral energy due to the mechanical perturbation.

The dispersion modeling procedure then followed the method introduced by Lee et al. [42]. Specifically, fifteen TMs $\{\mathbf{T}_{i, \text{narrow}}(\omega)\}_{i=1}^{15}$ were measured at wavelength intervals linear in optical frequency, centered around 1310 nm. The spacing between successive TMs was

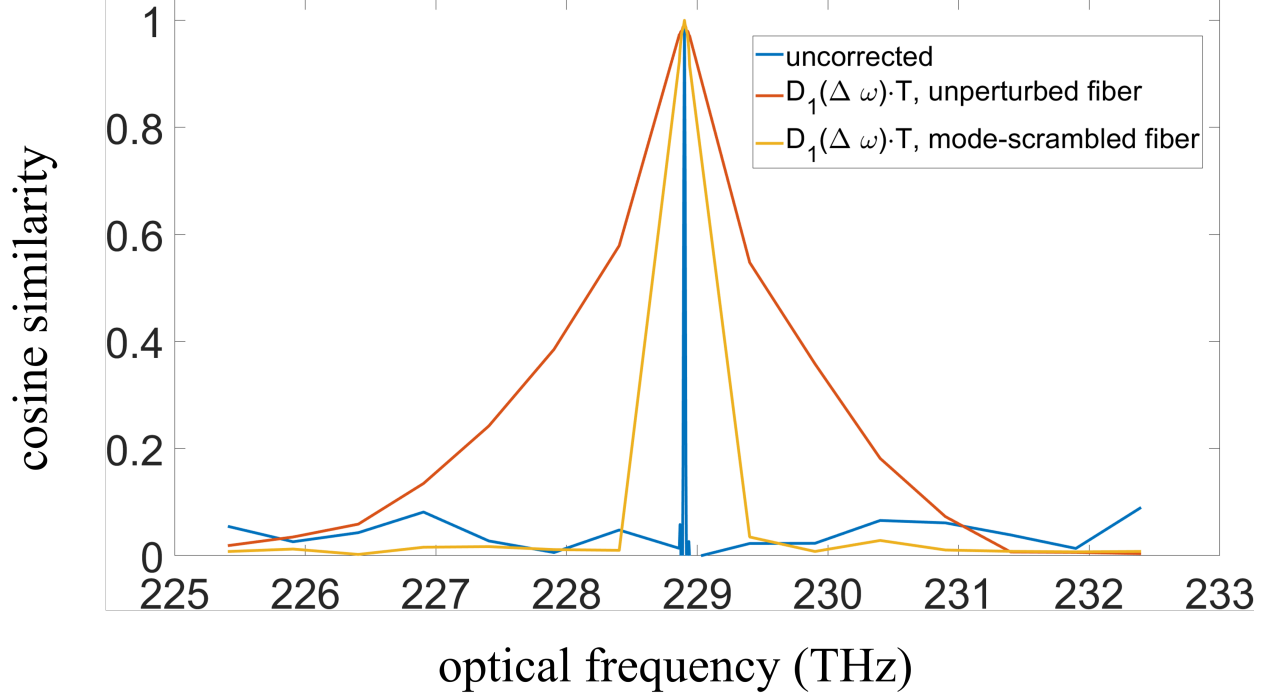


Figure 4.3: Effect of fiber normality on first-order dispersion model accuracy. The plot shows cosine similarity with the central TM, \mathbf{T}_8 as a function of wavelength for the MMF msTM. The blue curve represents the uncorrected msTM cosine similarity, while the orange and yellow curves correspond to the first-order dispersion-corrected TMs, $\mathbf{D}(\Delta\omega) \cdot \mathbf{T}_8$, for the unperturbed and mode-scrambled fiber, respectively. Mechanical compression introduced by the fiber-optic mode scrambler reduces the spectral correlation bandwidth of the first-order model, suggesting necessity of higher-order Magnus expansion terms that arise due to non-normality.

approximately 5.61 GHz—less than half the spectral decorrelation bandwidth of the MMF—to unambiguously observe phase change of the eigenvalues in the differential matrix. This yielded an overall spectral window from 1309.775 nm to 1310.225 nm. All TMs were projected onto the basis defined by the leading 320 singular vectors as $\mathbf{S}_i(\omega) = \mathbf{U}^\dagger \cdot \mathbf{T}_{i, \text{narrow}} \cdot \mathbf{V}$, corresponding to the number of non-evanescent modes in the fiber determined by a 5% threshold on the singular value spectrum. The matrices \mathbf{U} and \mathbf{V} were commonly defined as the right and left singular vectors of the eighth TM in the set, such that $\mathbf{T}_{8, \text{narrow}} = \mathbf{U} \cdot \mathbf{S}_8 \cdot \mathbf{V}^\dagger$ is its singular value decomposition. Global phase alignment was performed across wavelengths to eliminate offsets between the \mathbf{S}_i s. The first-order dispersion correction operator over this narrow spectral band was then computed as the solution to the least squares problem that assumed a constant $\mathbf{D}_1(\Delta\omega)$ between consecutive \mathbf{S}_i [42]:

$$\mathbf{D}_1 = \left(\sum_{i=1}^{N-1} \mathbf{S}_{n+1} \mathbf{S}_n^\dagger \right) \left(\sum_{i=1}^{N-1} \mathbf{S}_n \mathbf{S}_n^\dagger \right)^{-1}, \quad (4.30)$$

from which the exponential generator was estimated:

$$\mathbf{X}_1 = \frac{\text{logm } \mathbf{D}_1}{\Delta\omega}, \quad (4.31)$$

where logm denotes the matrix logarithm.

To evaluate the validity of the first order model over a broader frequency range, a subsequent set of 15 msTMs $\{\mathbf{T}_{i, \text{broad}}\}_{i=1}^{15}$, sampled linearly in optical frequency between wavelengths of 1290 nm and 1330 nm, was collected and projected onto the basis defined by \mathbf{U} and \mathbf{V} . This corresponded to $\mathbf{T}_{i, \text{broad}}$ spaced by approximately 0.500 THz between 225.4 THz and 232.4 THz. For each $\mathbf{T}_{i, \text{broad}}$, the dispersion-correction matrix \mathbf{D}_i was formed by exponentiating the scaled generator by the frequency difference from the reference TM, $\mathbf{T}_{8, \text{narrow}}$:

$$\mathbf{D}_i = e^{\mathbf{X}_1 \cdot (\omega_i - \omega_8)}. \quad (4.32)$$

The cosine similarity between $\mathbf{D}_i \cdot \mathbf{S}_{8, \text{narrow}}$ and $\mathbf{S}_{i, \text{broad}}$ was then calculated to evaluate the fidelity of the first-order dispersion-correction model and plotted in Fig. 4.3.

The observed results suggest that mechanical perturbation decreases the spectral correlation bandwidth of the first-order dispersion-correction model, as shown in Fig. 4.3. Before introduction of the fiber optic mode-scrambler, the correlation bandwidth at 0.5 cosine similarity is approximately 8 nm, but this bandwidth shrinks to less than 2 nm after scrambling. The reduction of the spectral correlation bandwidth and spectral energy metric indicates that parametric dispersion models break down in the presence of non-normality, since TMs at neighboring optical frequencies no longer form a commuting normal family. Thus, normality provides a mathematical criterion for when such models remain valid, as it governs the degree to which the TMs at different frequencies can be approximately jointly diagonalized in a stable eigenbasis.

Since the parametric dispersion model can be expressed as a first-order Magnus expansion, deviations from this approximation correspond to higher-order correction terms from the BCH formula, which arise precisely from this noncommutativity between TMs at neighboring frequencies. From this perspective, the higher-order BCH-correction terms in the Magnus expansion account for both frequency-dependent shifts in the eigenvectors of \mathbf{T}_ω and enhanced mode mixing, either of which lowers the achievable correlation bandwidth by decreasing the commutation between TMs at nearby frequencies. The mode scrambler plausibly introduces both effects: it accelerates shifts in the eigenbasis while simultaneously increasing modal crosstalk. Physically, this arises because fiber compression increases sensitivity to optical path length fluctuations, so that even small changes in wavelength lead to larger phase variations across modes. Together, these mechanisms generate the noncommutative BCH error that undermines the fidelity of the first-order Magnus approximation.

Chapter 5

Discussion and Future Work

Reciprocity and matrix normality impose independent yet complementary constraints on the structure of scattering operators. Reciprocity arises from the symmetry of the wave equation under source-observer interchange and applies universally to all linear, source-free systems. Matrix normality, by contrast, reflects an energy-conserving modal structure with orthogonal eigenchannels, and typically arises only in structured media such as waveguides or cavities. While reciprocity constrains the relation between input and output fields, normality captures their coherent transport in orthogonal channels.

This distinction was evident in analysis of the simultaneous preservation of normality and reciprocity in MMF TMs. In particular, reciprocity-driven correction of the single-pass MMF TM by enforcing $\mathbf{T}_{2\times} \approx \mathbf{T}_{\text{fw}}^T \cdot \mathbf{T}_{\text{fw}}$ did not appear to change the normality of \mathbf{T}_{fw} . This is expected: the transpose-product operation discards information about the directional mapping between input and output, instead only encoding overlap between channels of the input basis of \mathbf{T}_{fw} and $\mathbf{T}_{2\times}$. As such, it masks any asymmetry in the single-pass eigenstructure and cannot adjust for discrepancies from normality. Robust reciprocity correction could hence be performed on \mathbf{T}_{fw} in the native spot-to-pixel basis. In contrast, $\mathbf{T}_{2\times}$, which is defined between a common input and output basis, proved sensitive to such basis mismatches. Reciprocity could not be restored unless the underlying double-pass operator was first made approximately normal — that is, unless both input and output were expressed in a shared basis. The failure of the optimization procedure to intrinsically resolve the modal basis misalignment was attributed to the nonlinear nature of the required transformation to obtain matching bases. In particular, the dominant mismatch was found to be a geometric scaling between the two, corresponding to a demagnification of the output image relative to the input. This transformation could not be captured by the left-multiplied, phase-only correction operators in the near- and far- fields employed here. Notably, the preservation of normality of $\mathbf{T}_{2\times}$ did not depend on the choice of basis, but rather on the alignment between input and output sampling. Expressing $\mathbf{T}_{2\times}$ in both pixel-to-pixel and spot-to-spot bases — the latter constructed by convolving the average point spread function of the input focus across the output camera image of the MMF’s proximal facet — yielded similarly normal $\mathbf{T}_{2\times}$. This suggests that normality emerges under any basis that captures the physical symmetry of excitation and detection bases.

The interpretation of normality as a physically meaningful, basis-dependent property offers insight into previous results. In particular, the method of aberration correction demonstrated

by Matthès et al. to deduce the mode-basis MMF TM [19] can be viewed through the lens of normality optimization. In their formulation, phase corrections composed of low-order Zernike terms are applied to maximize the energy captured in the TM when expressed in a predefined mode basis. Implicit in this procedure is the assumption that, in the correct basis, i.e., after removal of spatial misalignments and aberrations, the MMF TM becomes approximately normal, with its energy concentrated in a set of orthogonal modes. As noted by Matthès et al., this corresponds to proper spatial alignment between their excitation using a digital micro-mirror device and output camera pixels. Their observation aligns with the present findings: that normality in MMFs is not an intrinsic property of the raw TM, but one that emerges under appropriate basis-matching. Matthès et al. observed that 92% of the energy was concentrated in the mode basis after optimization, in agreement with the results presented here.

Normality also offers an explanation for the existence and robustness of the deformation-resistant channels reported by Matthès et al. [19]. In that work, the generalized Wigner–Smith operator [15] was used to approximate the response of the MMF TM to external perturbations, such as bending. The deformation response was estimated via finite-difference approximations across deformation states, and eigenchannels with minimal drift were identified. From the perspective of matrix analysis, a well-behaved finite-difference derivative implies spectral stability, which is closely tied to matrix normality. As discussed by Henrici, Trefethen and Embree [37, 54], normal matrices exhibit smooth spectral variation under perturbations, whereas non-normal matrices may display large changes in eigenstructure in response to small changes in the operator. In this context, the ability of Matthès’ method to identify deformation-resistant channels likely reflects the underlying near-normality of the MMF TM, once the system is sampled in an appropriate basis. Absent normality, there is no formal guarantee that such eigenchannels remain meaningful or stable under deformation, wavelength variation, or environmental fluctuations. By extension, this reasoning also applies to efficient methods for modeling dispersion [42] based on smooth spectral variation of the TMs of modal complex media. This reinforces the interpretation of normality not merely as a mathematical artifact, but as a relevant descriptor of transport behavior in structured systems.

The emergence of approximate normality in certain scattering media further points to algebraic and geometric structure. Commuting normal matrices form a closed, abelian subgroup of the general linear group $GL(n, \mathbb{C})$ [67]. By Cartan’s theorem, any closed subgroup of a Lie group is itself a Lie group and therefore possesses a smooth manifold structure [67]. This implies that families of jointly normal, commuting scattering operators trace continuous trajectories on a differentiable manifold, generated by their shared Lie algebra through the matrix exponential. As a result, the evolution of such systems under external parameters, whether frequency, spatial deformation, or boundary perturbation, can be understood as geodesic flow along this manifold. This geometric perspective may enable new modes of analysis and control, in which transformations of complex media may be interpreted as motion through a structured mathematical space.

The matrix normality observed here is a manifestation of deeper structure in the underlying Green’s operator of the system. For time-harmonic wave equations in linear, source-free media, the Green’s operator encodes the system’s full input–output behavior [2]. For modal systems, the Green’s operator may be expanded in an orthonormal basis of eigenfunctions. Energy propagating through the system is projected into the basis of these modes, which do

not mutually interfere. In contrast, disordered or absorptive media correspond to Green’s operators that may not be expressible in an eigenvalue expansion, leading to non-normal scattering behavior. When a scattering matrix is measured, however, this property may not be obvious. If, as in experimental systems, illumination and detection channel are not perfectly matched, the apparent normality of the system is degraded: an eigenmode launched in one basis at the input, if not carefully matched to the detection basis, will appear to mix into others at the output, even in modal systems like MMF.

The appearance of normality in structured systems such as multimode fibers reflects an underlying orthogonality of the modal basis, and thus serves as an operational fingerprint of separable, energy-conserving transport. In contrast, the pronounced non-normality observed in the reflection matrices of scattering slabs suggests a breakdown of this orthogonality, consistent with the presence of lossy, interfering, or multiply degenerate paths. In this sense, matrix normality may be viewed as a structural order parameter for transport regimes, distinguishing coherent modal propagation from incoherent or dissipative behavior. These observations are aligned with ongoing developments in non-Hermitian physics, where deviations from Hermiticity — and, more generally, from normality — give rise to phenomena such as spectral instability, exceptional points, and non-reciprocal mode coupling. Unlike Hermiticity, however, normality does not enforce energy conservation, but rather modal separability; its breakdown, therefore, highlights a transition not necessarily to loss, but to coupling among eigenchannels. As such, the normality framework developed here may offer a physically grounded criterion for identifying the onset of mode-mixing in open systems, and for guiding the design of stable inverse scattering methods and compressive measurement protocols. When used in tandem with reciprocity constraints, this approach provides a unified matrix-theoretic lens through which to view coherent transport across media ranging from waveguides to disordered scattering systems. The underlying framework may also find relevance in quantum transport and in the engineering of metasurfaces, where tailoring modal interactions and ensuring spectral stability are essential for coherent control and design precision.

In conclusion, a matrix-based framework is presented for assessing and correcting system-level aberrations in complex optical systems. Reciprocity serves as a calibration constraint, enabling correction in non-reciprocal paths and across diverse sample types without reliance on a predefined modal basis. Matrix normality emerges as a structural descriptor: near-normality corresponds to orthogonal transport channels and spectral stability, whereas non-normality signals mode mixing and spectral fragility. Experimental measurements in multimode fibers and disordered slabs confirmed this contrast, with pseudospectral analysis and Henrici departure quantifying the deviations. Normality further governs dispersion behavior: in nearly normal fibers the Wigner–Smith operator remains jointly diagonalizable and first-order models capture wavelength variation, while in perturbed fibers the loss of normality leads to noncommuting operators, breakdown of Magnus-series corrections, and a subsequent collapse of fidelity of the first-order model. Beyond imaging and fiber transport, the diagnostic role of normality points to applications in wavefront shaping, operator compression, inverse design, and the study of eigenchannel stability in quantum and photonic media.

References

- [1] M. Born and E. Wolf, *Principles of optics*, 4th (Pergamon Press, 1970).
- [2] P. M. Morse and H. Feshbach, *Methods of theoretical physics* (McGraw-Hill, New York, Toronto, London, 1953).
- [3] C. W. J. Beenakker, *Rev. Mod. Phys.* **69**, 731–808 (1997).
- [4] P. A. Lee and A. D. Stone, *Physical Review Letters* **55**, 1622–1625 (1985).
- [5] H. Mathur and A. D. Stone, *Physical Review Letters* **68**, 2964–2967 (1992).
- [6] C. W. J. Beenakker, *Physical Review Letters* **81**, 1829–1832 (1998).
- [7] S. Feng, C. Kane, P. A. Lee, and A. D. Stone, *Physical Review Letters* **61**, 834–837 (1988).
- [8] W. J. Skocpol, P. M. Mankiewich, R. E. Howard, L. D. Jackel, D. M. Tennant, and A. D. Stone, *Physical Review Letters* **56**, 2865–2868 (1986).
- [9] H. A. Haus, *Waves and fields in optoelectronics* (Prentice Hall, 1984).
- [10] S. Rotter and S. Gigan, *Rev. Mod. Phys.* **89**, 015005 (2017).
- [11] I. M. Vellekoop and A. P. Mosk, *Opt. Lett.* **32**, 2309–2311 (2007).
- [12] S. M. Popoff, G. Lerosey, R. Carminati, M. Fink, A. C. Boccarda, and S. Gigan, *Physical Review Letters* **104**, 100601 (2010).
- [13] S. Popoff, G. Lerosey, M. Fink, A. C. Boccarda, and S. Gigan, *Nature Communications* **1**, 81 (2010).
- [14] S. Popoff, A. Aubry, G. Lerosey, M. Fink, A. Boccarda, and S. Gigan, *Phys. Rev. Lett.* **107**, 263901 (2011).
- [15] P. Ambichl, A. Brandstötter, J. Böhm, M. Kühmayer, U. Kuhl, and S. Rotter, *Physical Review Letters* **119**, 033903 (2017).
- [16] H. Cao, T. Čižmár, S. Turtaev, T. Tyc, and S. Rotter, *Adv. Opt. Photonics* **15**, 524–612 (2023).
- [17] M. Plöschner, T. Tyc, and T. Čižmár, *Nat. Photonics* **9**, 529–535 (2015).
- [18] J. Carpenter, B. J. Eggleton, and J. Schröder, *Nat. Photonics*, 10.1038/nphoton.2015.164 (2015).
- [19] M. W. Matthès, Y. Bromberg, J. de Rosny, and S. M. Popoff, *Phys. Rev. X* **11**, 021060 (2021).

- [20] Y. Choi, C. Yoon, M. Kim, T. D. Yang, C. Fang-Yen, R. R. Dasari, K. J. Lee, and W. Choi, *Physical Review Letters* **109**, 203901 (2012).
- [21] T. Čižmár and K. Dholakia, *Nature Communications* **3**, 1027 (2012).
- [22] Z. Wen et al., *Nat. Photonics* **17**, 679–687 (2023).
- [23] G. S. D. Gordon, M. Gataric, A. G. C. P. Ramos, R. Mouthaan, C. Williams, J. Yoon, T. D. Wilkinson, and S. E. Bohndiek, *Phys. Rev. X* **9**, 041050 (2019).
- [24] Y. Zheng, T. Wright, Z. Wen, Q. Yang, and G. S. D. Gordon, *Communications Physics* **6**, 306 (2023).
- [25] S. Leedumrongwatthanakun, L. Innocenti, H. Defienne, T. Juffmann, A. Ferraro, M. Paternostro, and S. Gigan, *Nature Photonics* **14**, 139–142 (2020).
- [26] H. Defienne, M. Barbieri, I. A. Walmsley, B. J. Smith, and S. Gigan, *Science Advances*, Published online 2016, 10.1126/sciadv.1600152 (2016).
- [27] P. Balondrade, V. Barolle, N. Guigui, E. Auriant, N. Rougier, C. Boccara, M. Fink, and A. Aubry, *Nature Photonics* **18**, 1097–1104 (2024).
- [28] A. Badon, V. Barolle, K. Irsch, A. C. Boccara, M. Fink, and A. Aubry, *Science Advances* **6**, eay7170 (2020).
- [29] Y.-R. Lee, D.-Y. Kim, Y. Jo, M. Kim, and W. Choi, *Nature Communications* **14**, 1878 (2023).
- [30] S. Yoon, H. Lee, J. H. Hong, Y.-S. Lim, and W. Choi, *Nature Communications* **11**, 5721 (2020).
- [31] H. von Helmholtz, *Handbuch der physiologischen optik [handbook of physiological optics]*, 1st, Vol. 1, p. 169; cited by Planck (Leopold Voss, Leipzig, 1856).
- [32] H. von Helmholtz, *Journal für die reine und angewandte Mathematik* **57**, p. 29, 1–72 (1859/1860).
- [33] H. von Helmholtz, *Vorlesungen über theorie der wärme*, edited by F. Richarz (Johann Ambrosius Barth, Leipzig, 1903), pp. 158–162.
- [34] J. W. Strutt, *Proceedings of the Royal Society A* **25**, 118–122 (1876).
- [35] J. W. Strutt, *Proceedings of the London Mathematical Society*, 4th ser. **4**, 357–368 (1873).
- [36] R. A. Horn and C. R. Johnson, *Matrix analysis* (Cambridge University Press, 1991).
- [37] P. Henrici, *Numerische Mathematik* **4**, 24–40 (1962).
- [38] E. P. Wigner, *Physical Review* **98**, 145–147 (1955).
- [39] F. J. Dyson, *Journal of Mathematical Physics* **3**, 1191–1198 (1962).
- [40] H. U. Baranger and P. A. Mello, *Physical Review Letters* **73**, 142–145 (1994).
- [41] F. T. Smith, *Physical Review* **118**, 349–356 (1960).
- [42] S.-Y. Lee, V. J. Parot, B. E. Bouma, and M. Villiger, *Light: Science & Applications* **12**, 31 (2023).

- [43] A. Yariv, *Optical electronics*, 2nd (Holt, Rinehart and Winston, 1984).
- [44] W. Xiong, C. W. Hsu, Y. Bromberg, J. E. Antonio-Lopez, R. A. Correa, and H. Cao, *Light: Science & Applications* **7**, 54 (2018).
- [45] J. B. Conway, *A course in functional analysis*, 2nd, Vol. 96, Graduate Texts in Mathematics (Springer, New York, 2007).
- [46] W. contributors, *Zernike polynomials*, Accessed: 2025-08-15, 2025.
- [47] E. CuChe, P. Marquet, and C. Depeursinge, *Applied Optics* **39**, 4070–4075 (2000).
- [48] S. M. Popoff, *Off-axis holography*, Wavefrontshaping.net blog post, Tutorial; includes MATLAB and Python example codes, Oct. 2013.
- [49] S.-Y. Lee, V. J. Parot, B. E. Bouma, and M. Villiger, *APL Photonics* **5**, 106104 (2020).
- [50] W. Wirtinger, German, *Mathematische Annalen* **97**, Available at DigiZeitschriften, 357–375 (1927).
- [51] H. Poincaré, French, *Acta Mathematica* **22**, 89–178 (1899).
- [52] K. Koor, Y. Qiu, L. C. Kwek, and P. Rebentrost, *A short tutorial on wirtinger calculus with applications in quantum information*, 2023.
- [53] K. B. Petersen and M. S. Pedersen, *The matrix cookbook*, <http://www.math.uwaterloo.ca/~hwolkowi/matrixcookbook.pdf>, Version November 15, 2012, 2008.
- [54] L. N. Trefethen and M. Embree, *Spectra and pseudospectra: the behavior of nonnormal matrices and operators* (Princeton University Press, Princeton, NJ, 2005).
- [55] J. Descloux, *Numerische Mathematik* **15**, 185–190 (1963).
- [56] J. A. Stratton and L. J. Chu, *Physical Review* **56**, 99–109 (1939).
- [57] T. G. Wright, *Eigtool*, <http://www.comlab.ox.ac.uk/pseudospectra/eigtool/>, 2002.
- [58] W. Magnus, *Communications on Pure and Applied Mathematics* **7**, 649–673 (1954).
- [59] S. Fan and J. M. Kahn, *Optics Letters* **30**, 135–137 (2005).
- [60] H. F. Baker, Proceedings of the London Mathematical Society, 1st ser. **34**, 347–360 (1902).
- [61] H. F. Baker, Proceedings of the London Mathematical Society, 1st ser. **35**, 333–374 (1903).
- [62] H. F. Baker, Proceedings of the London Mathematical Society, 2nd ser. **3**, 24–47 (1905).
- [63] J. E. Campbell, Proceedings of the London Mathematical Society, 1st ser. **28**, 381–390 (1897).
- [64] J. E. Campbell, Proceedings of the London Mathematical Society, 1st ser. **29**, 14–32 (1898).
- [65] F. Hausdorff, Berichte über die Verhandlungen der Sächsischen Akademie der Wissenschaften zu Leipzig, Mathematisch-Physikalische Klasse **58**, 19–48 (1906).
- [66] M. Suzuki, *Journal of Mathematical Physics* **26**, 601–612 (1985).
- [67] B. C. Hall, *Lie groups, lie algebras, and representations: an elementary introduction*, 2nd, Vol. 222, Graduate Texts in Mathematics (Springer, New York, 2015).